

# The Intrinsic 150-day Periodicity of the Southern Hemisphere Extratropical Large-Scale Atmospheric Circulation

Sandro W. Lubis<sup>1\*</sup> and Pedram Hassanzadeh<sup>1</sup>

<sup>1</sup>Rice University, Houston, TX, 77005, USA

## Key Points:

- We show using theory, reanalysis data, and model hierarchy that the Southern Annular Mode has an internally generated 150-day periodicity
- Periodicity is tied with the annular mode's propagating regime, and affects hemispheric-scale precipitation and ocean surface wind stress
- CMIP models vary in how well they reproduce the periodicity; new metrics are introduced to evaluate these models and understand their biases

---

\*Current address: Pacific Northwest National Laboratory, Richland, WA, 99354, USA

Corresponding author: Sandro W. Lubis and Pedram Hassanzadeh, [sandro.lubis@pnnl.gov](mailto:sandro.lubis@pnnl.gov); [pedram@rice.edu](mailto:pedram@rice.edu)

## Abstract

The variability of the Southern Hemisphere (SH) extratropical large-scale circulation is dominated by the Southern Annular Mode (SAM), whose timescale is extensively used as a key metric in evaluating state-of-the-art climate models. Past observational and theoretical studies suggest that the SAM lacks any internally generated (intrinsic) periodicity. Here, we show, using observations and a climate model hierarchy, that the SAM has an intrinsic 150-day periodicity. This periodicity is robustly detectable in the power spectra and principal oscillation patterns (aka dynamical mode decomposition) of the zonal-mean circulation, and in hemispheric-scale precipitation and ocean surface wind stress. The 150-day period is consistent with the predictions of a new reduced-order model for the SAM, which suggests that this periodicity is tied with a complex interaction of turbulent eddies and zonal wind anomalies, as the latter propagate from low to high latitudes. These findings present a rare example of periodic oscillations arising from the internal dynamics of the extratropical turbulent circulations. Based on these findings, we further propose a new metric for evaluating climate models, and show that some of the previously reported shortcomings and improvements in simulating SAM's variability connect to the models' ability in reproducing this periodicity. We argue that this periodicity should be considered in evaluating climate models and understanding the past, current, and projected Southern Hemisphere climate variability.

## Plain Language Summary

The Southern Annular Mode (SAM), which involves hemispheric-scale north-south movement of the midlatitude jet stream, dominates the variability of the Southern Hemisphere (SH) large-scale atmospheric circulation. The SAM has extensive impacts on the Southern Ocean and Antarctica, and the past, current, and future climate of the SH is often viewed through the lens of the SAM. Studies since early 1990s suggested that SAM's variability lacks any internally generated periodic oscillation, as expected from the turbulent and thus chaotic nature of the midlatitude circulation. However, here we show using observational data, model data, and theory that SAM has an intrinsic 150-day periodicity arising from the internal dynamics of the extratropical atmosphere. This 150-day oscillation clearly influences the variability of the hemispheric-scale precipitation and ocean surface wind stress, suggesting broader impacts of this periodicity on the SH weather and climate. We also found that many state-of-the-art climate models cannot faithfully reproduce this periodicity, providing an explanation for some of the previously reported shortcomings of these models in simulating SAM's variability. Based on these findings, we propose new metrics and ideas for evaluating these models and understanding their shortcomings, and potentially, improving them.

## 1 Introduction

The variability of the Southern Hemisphere extratropical large-scale atmospheric circulation on intraseasonal to interannual timescales is dominated by the Southern Annular Mode (SAM). The SAM describes hemispheric-scale, north-south fluctuations in the extratropical circulation throughout the troposphere and lower stratosphere, and it is often defined as the leading empirical orthogonal function (EOF) of zonally averaged meteorological fields such as the daily zonal wind (Kidson, 1988; Lorenz & Hartmann, 2001; G. J. Marshall, 2003). The SAM has significant impacts on the Southern Hemisphere's weather and climate; for example, it is linked to variations in the temperature, precipitation, sea ice, stratospheric ozone, and carbon cycle, as well as the surface wind stress across the Southern Ocean and the distribution of cloudiness around the perimeter of Antarctica (Hall & Visbeck, 2002; Thompson & Solomon, 2002; Gillett et al., 2006; Ceppi & Hartmann, 2015; A. G. Marshall et al., 2018; Hell et al., 2021). The effects of past, current, and projected climate change on large-scale circulation in the Southern

Hemisphere and the resulting impacts on the ocean, cryosphere, and biogeochemical cycle are also often interpreted and connected through the structure and timescale of the SAM (Thompson & Solomon, 2002; Kushner et al., 2001; Gillett & Fyfe, 2013; Chiang et al., 2018; Banerjee et al., 2020). Furthermore, the fidelity of global climate models (GCMs) in simulating the spatio-temporal characteristics of the SAM compared to observations is one of the key metrics used to evaluate GCMs, particularly those in Coupled Model Intercomparison Project, CMIP (Gerber, Voronin, & Polvani, 2008; Simpson & Polvani, 2016; Bracegirdle et al., 2020; Simpson et al., 2020; Morgenstern, 2021; J. Lee et al., 2021). As a result, understanding the dynamics, spatio-temporal variabilities, and trends of the SAM is of substantial importance and has been an active area of research since the early 1990s.

Past studies suggest that the temporal variability of the SAM is driven by variations in forcing from eddy momentum fluxes acting on the leading EOF of zonal-mean zonal wind, referred to as EOF1 hereafter (Robinson, 1991; S. Feldstein & Lee, 1998; Robinson, 2000; Lorenz & Hartmann, 2001; Gerber & Vallis, 2007; Chen & Plumb, 2009; Limpasuvan et al., 2012; Simpson et al., 2013b; Byrne et al., 2016; Nie et al., 2014; Ma et al., 2017; Boljka et al., 2018; Hassanzadeh & Kuang, 2019; Lutsko & Hell, 2021). Lorenz and Hartmann (2001) introduced an elegant reduced-order model for the variability of EOF1 and this feedback between the zonal-mean flow and eddy forcing. Consistent with this reduced-order model of the SAM (referred to as LH01 hereafter; to be discussed in Section 3.3), reanalysis data and comprehensive GCM simulations show that the spectrum of the time-series of the SAM, i.e., the principal component (PC) of EOF1 (sometimes called the *zonal index*), follows a normally distributed red-noise process, lacking any noticeable periodicity or quasi-periodicity (Lorenz & Hartmann, 2001; Ma et al., 2017; S. B. Feldstein, 2000).

This observation has not been surprising. While periodic and quasi-periodic variabilities exist in the global climate system as a result of astronomical/orbital forcings (e.g., the seasonal cycle, Milankovic cycle, and solar cycle) and exist in the tropical atmosphere (Madden-Julien Oscillation and Quasi-Biennial Oscillation, QBO) and atmosphere-ocean coupled system (El Niño-Southern Oscillation, ENSO), *internally generated* variabilities in the extratropical atmosphere typically have red spectra, consistent with the turbulent and thus chaotic nature of the extratropical troposphere (Mitchell, 1976; Hartmann, 2016). However, a notable exception was found recently: Thompson and Barnes (2014) showed that in the Southern Hemisphere extratropical circulation, the PC of the leading EOF of the zonal-mean eddy kinetic energy (EKE), which is called the baroclinic annular mode (BAM) and is distinct from the SAM (Thompson & Barnes, 2014; Thompson & Woodworth, 2014), has a noticeable 20- to 30-day periodicity in reanalysis data and a hierarchy of GCMs. They developed a reduced-order model for the BAM, showing that the periodicity arises from the feedbacks between the baroclinicity and the eddy heat flux associated with the leading EOF of the EKE. Nonetheless, it has remained the general understanding that unlike the BAM, the SAM has no intrinsic periodicity. That said, a little noticed 1994 paper by P. M. James et al. (1994) based on a very idealized GCM, recent work by Sheshadri and Plumb (2017), based on a principal oscillation pattern (POP), also known as dynamic mode decomposition (DMD), and theoretical predictions from a newly developed reduced-order model of SAM by Lubis and Hassanzadeh (2021) implied—but did not further examine—that the SAM might have a  $\sim 150$ -day periodicity.

In this paper, we show unambiguously, for the first time, that the SAM indeed has an ultra-long  $\sim 150$ -day periodicity, which is distinct from the periodicity of the BAM (in terms of the timescale and mechanism). This periodicity is robustly detectable in the spectra of the zonal index and through the POP/DMD analysis of reanalysis datasets and of simulations from a hierarchy of idealized to comprehensive GCMs. We demonstrate that this periodicity is consistent with the theoretical predictions of the new reduced-

order model of Lubis and Hassanzadeh (2021), which suggests that this periodicity is *internally generated* in the extratropical atmosphere and is associated with the *propagating regime* (Riehl et al., 1950; S. B. Feldstein, 1998; Son & Lee, 2006; Son et al., 2008; Sparrow et al., 2009; Sheshadri & Plumb, 2017) of the SAM (the distinction between the propagating and non-propagating annular modes will be discussed in Section 3.3). Based on this new model, not only the two leading EOFs of the zonal-mean zonal wind (EOF1 and EOF2) have feedbacks on themselves, as already suggested by Lorenz and Hartmann (2001), but they also exert feedbacks on each other through varying eddy momentum fluxes (i.e., cross-EOF feedbacks) at lag times of around 10–20 days. The  $\sim 150$ -day periodicity is closely tied to the existence of cross-EOF feedbacks (Lubis & Hassanzadeh, 2021).

We also show that this  $\sim 150$ -day periodicity has a clear signature in the variability of hemispheric-scale precipitation and the ocean surface wind stress, suggesting broader impacts on the climate variability of the Southern Hemisphere. Furthermore, we demonstrate that how well the propagating regime and this periodicity are simulated by CMIP5 and CMIP6 models significantly affects the persistence of SAM in these GCMs. Based on this, we propose a new metric for evaluating state-of-the-art climate models and potentially improving them.

## 2 Materials and Methods

### 2.1 Reanalysis Datasets: ERA5, MERRA2, NCEP1, and NCEP2

We use 6-hourly horizontal wind and precipitation data from the European Center for Medium-Range Weather Forecasts (ECMWF) ERA5 reanalysis dataset (Hersbach et al., 2020) for the period from January 1979 to December 2020. We use the data with a horizontal resolution of  $1^\circ$  latitude  $\times$   $1^\circ$  longitude from 27 pressure levels between 1000 and 100 hPa. The ERA5 precipitation is a model-derived quantity; however, it is calculated using physically consistent parameterizations that link atmospheric motions to precipitation (Hersbach et al., 2020). In addition, we also use daily zonal and meridional wind stress data from NCEP1 with a resolution of  $2.5^\circ$  latitude  $\times$   $2.5^\circ$  longitude. The data are provided from January 1979 to December 2020.

For these variables (and any other variable in this paper), anomalies are computed by removing the mean seasonal cycle (except in the idealized GCM; in this case, the long-term mean is removed, as there is no seasonal cycle). The mean seasonal cycle is defined as the annual average and the first four Fourier harmonics of the daily climatology at each grid point (Lorenz & Hartmann, 2001). Removing the seasonal cycle using a different approach, based on a 21-day running mean climatology (Sheshadri & Plumb, 2017), yielded the same results and conclusions.

We also employ 6-hourly horizontal wind data from 1980–2020 from MERRA2 (Bosilovich et al., 2015) with a spatial resolution of  $1.25^\circ$  latitude  $\times$   $1.25^\circ$  longitude, and from 1979–2020 from NCEP1 (Kalnay et al., 1996) and NCEP2 (Kanamitsu et al., 2002) with a spatial resolution of  $2.5^\circ$  latitude  $\times$   $2.5^\circ$  longitude.

### 2.2 CMIP5 and CMIP6 Datasets

We use data from two phases of the Coupled Model Intercomparison Project (CMIP): CMIP5 (Taylor et al., 2012) and CMIP6 (Eyring et al., 2016). We use the daily averaged zonal wind at 500 hPa from 24 CMIP5 models and 20 CMIP6 models from “historical” simulations for the period from 1960–2005. A complete list of the CMIP models is reported in Tables S3 and S4.

### 2.3 Idealized GCM Simulations

We use 6-hourly horizontal wind data from simulations of two setups of the Geophysical Fluid Dynamics Laboratory (GFDL) dry dynamical core GCM with a flat, uniform lower boundary. For both setups, the GCM is integrated with a T63 spectral resolution and 40 evenly spaced sigma levels in the vertical direction for 100000 days after a 1000-day spin-up. In one setup, the parameter settings, forcing, and dissipation are identical to those in the “Held-Suarez benchmark” (Held & Suarez, 1994) in which an analytical profile approximating a troposphere in unstable radiative-convective equilibrium and an isothermal stratosphere are used in the Newtonian relaxation scheme (with an equinoctial condition). The annular mode in this setup is in the non-propagating regime (as shown in Fig. 5). It is known that this setup’s annular mode is overly persistent (compared to the reanalysis), which had been often attributed to a too-strong EOF1-onto-EOF1 positive feedback in past studies (Chen & Plumb, 2009; Hassanzadeh & Kuang, 2019). Recently, Lubis and Hassanzadeh (2021) showed that the too-persistent annular mode in this setup is at least partly (if not entirely) due to the lack of cross-EOF feedbacks.

The second setup is identical to the one used in Lubis and Hassanzadeh (2021) and follows the approach of Sheshadri and Plumb (2017). In this setup, we prescribe diabatic heating by relaxing the temperature (in the troposphere and stratosphere) toward realistic background temperature equilibrium fields based on rapid radiative transfer mode (RRTM) calculations. The GCM’s southern (northern) hemisphere is in perpetual winter (summer). These choices result in a more realistic climatological large-scale circulation. The annular mode in this setup is in the propagating regime (as shown later in Fig. 5), and it has reasonable timescales in its southern hemisphere compared to the reanalysis.

Note that as shown in Fig. S5, in the first setup (non-propagating), the climatological circulation has a single jet and the ratio of the explained variance of EOF1 to that of EOF2 is 3.1. In the second setup (propagating), there is a double-jet structure and the ratio is 1.2, which is consistent with the rule of thumb for the existence of the annular mode’s propagating regime identified by past studies: EOF1 and EOF2 should have an explained variance ratio of  $< 2$  and there should be a double-jet structure (Son & Lee, 2006; Son et al., 2008; Hassanzadeh & Kuang, 2016).

### 2.4 A CESM-WACCM Simulation

In order to further support the results from the reanalysis datasets and idealized GCMs, we also use 100-year simulation data from NCAR’s Community Earth System Model (CESM) version 2. This is a state-of-the-art fully coupled model, which includes interactive ocean, land, and sea-ice components, and an atmospheric component with interactive chemistry (WACCM) version 6 (Gettelman et al., 2019). WACCM has a finite-volume dynamical core with standard 70 vertical levels (from the surface up to 140 km or  $\sim 5.1 \times 10^{-6}$  hPa) and a horizontal resolution of  $0.9^\circ$  latitude  $\times$   $1.25^\circ$  longitude. WACCM includes interactive chemistry and radiation. The QBO is internally generated in the model. The greenhouse gases and ozone-depleting substances are kept constant at the present-day conditions, allowing us to study the Southern Hemisphere variability isolated from any anthropogenic influence.

### 2.5 EOF Analysis and Calculation of Zonal Indices $z_i$ and Eddy Forcings $m_i$

Before calculating the EOFs, the vertically averaged, zonal-mean zonal wind anomalies from  $20^\circ\text{S}$  to  $80^\circ\text{S}$  are calculated. The vertical average is taken from the surface up to 200 hPa to account for only the tropospheric variability. These fields are then weighted

by the square root of the cosine of the latitude  $\phi$  to account for the decrease in area toward the pole (Simpson et al., 2013a; Lubis & Hassanzadeh, 2021).

After calculating the EOFs, the zonal indices ( $z_1$  and  $z_2$ ) and time-series of eddy forcing ( $m_1$  and  $m_2$ ) are calculated as the projection of the vertically averaged ( $\langle \cdot \rangle$ ) zonal-mean ( $\bar{\cdot}$ ) zonal wind  $\langle \bar{u} \rangle$  anomalies and vertically averaged zonal-mean eddy momentum flux convergence  $\langle \bar{F} \rangle$  anomalies onto the leading EOFs of  $\langle \bar{u} \rangle$  anomalies (Lorenz & Hartmann, 2001; Simpson et al., 2013a; Ma et al., 2017; Lubis & Hassanzadeh, 2021):

$$z_j(t) = \frac{\langle \bar{u} \rangle(t) \mathbf{W} \mathbf{e}_j}{\sqrt{\mathbf{e}_j^T \mathbf{W} \mathbf{e}_j}}, \quad (1)$$

$$m_j(t) = \frac{\langle \bar{F} \rangle(t) \mathbf{W} \mathbf{e}_j}{\sqrt{\mathbf{e}_j^T \mathbf{W} \mathbf{e}_j}}, \quad (2)$$

where  $j = 1$  or  $2$ .  $z_j$  ( $m_j$ ) is the component of the field  $\langle \bar{u} \rangle$  ( $\langle \bar{F} \rangle$ ) that projects onto the latitudinal structure of the  $j^{\text{th}}$  EOF,  $\mathbf{e}_j$ . Superscript T indicates the transpose.  $\langle \bar{u} \rangle(t)$  and  $\langle \bar{F} \rangle(t)$  are  $\langle \bar{u} \rangle(\phi, t)$  and  $\langle \bar{F} \rangle(\phi, t)$  with their latitude dimension vectorized, and  $\mathbf{W}$  is a diagonal matrix whose elements are the  $\cos(\phi)$  weighting used when defining the EOF structure. Here,  $\langle \bar{F} \rangle$  is calculated as the convergence of the vertically averaged zonal-mean eddy momentum flux:

$$\langle \bar{F} \rangle(\phi, t) = -\frac{1}{\cos^2 \phi} \frac{\partial(\langle \bar{u}'v' \cos^2 \phi \rangle)}{a \partial \phi}, \quad (3)$$

where primes are deviations from zonal means and  $a$  is the Earth's radius. All data used in Eqs. (1)–(3) are daily means (averaged from 6-hourly data); note that the eddy fluxes are first computed using 6-hourly data and then averaged daily.

As for CMIP models, because 6-hourly zonal wind data at all pressure levels were not archived for the CMIP5 and CMIP6 models, the modes are defined by calculating the first EOF of the daily, deseasonalized, latitude-weighted, 500-hPa zonal-mean zonal wind anomalies between 20°S and 80°S, following Gerber, Polvani, and Ancukiewicz (2008) and Bracegirdle et al. (2020). In ERA5, annular mode indices based on this definition are highly correlated with indices based on the vertically averaged, zonal-mean zonal wind anomalies (the average correlation is 0.996 in the Southern Hemisphere).

### 3 Results

#### 3.1 The Intrinsic 150-day Periodicity of the SAM

Figure 1a shows that the power spectrum of the SAM's zonal index ( $z_1$ ) in the 1979–2020 ERA5 reanalysis dataset has a noticeable peak at around 150 days. This spectral peak in ERA5 is robust to changes in the time period (including 1950–2020) and parameters used for estimating the spectrum (see Fig. S1). Similar peaks at  $\sim 150$  days are seen in the  $z_1$  spectra of 3 other reanalysis products (Fig. S2) and of CESM-WACCM, a fully coupled Earth system model (Fig. 1b). Among two specific setups of an idealized GCM (a dry dynamical core), the  $z_1$  spectrum of one setup has a prominent peak at  $\sim 150$  days (Fig. 1c), while the spectrum of the other setup lacks any peak and is red (Fig. 1d). As discussed later, the difference between these two setups is that the annular mode of the former (latter) setup is in the propagating (non-propagating) regime.

To provide further evidence for the 150-day periodicity, we perform a POP/DMD analysis (Penland, 1989; Tu et al., 2014; Khodkar & Hassanzadeh, 2018). Unlike EOFs, which are purely statistical entities, the POP/DMD modes have close connections to the system's dynamics, even for nonlinear systems (see Appendix A). The POP/DMD modes



**Table 1.** Periodicity of the SAM in the ERA5 reanalysis, two idealized GCM setups, and CESM-WACCM. The second column shows the periodicity predicted by the theoretically derived Eq. (7) given the estimates of  $b_{jk}$  and  $\tau_j$  in Table 2. The 25th and 75th percentiles provide a measure of the uncertainty with respect to the choice of the lag time  $\ell$  in estimating  $b_{jk}$  (see the Supporting Information for details). The third column shows the periodicity associated with the peak of the  $z_1$  spectrum in Figs. 1a, b and S2d. The last column shows the periodicity of the leading POP/DMD mode, computed as  $2\pi\lambda_I^{-1}$ , where  $\lambda_I$  is the imaginary part of the eigenvalue (Eq. (A9)). See Appendix A for more details about the POP/DMD calculations. Note that for the idealized GCM with a non-propagating regime, Eqs. (6) and (7) predict no periodicity (Table 2), there is no peak in the  $z_1$  spectrum (Fig. 1c), and the leading POP/DMD mode is a real number ( $\lambda_I = 0$ ). Supplementary Table S1 shows the same analysis but for three other reanalysis products.

Data	Periodicity predicted by Eq. (7) (25 <sup>th</sup> , mean, 75 <sup>th</sup> ) (days)	Periodicity at the peak of $z_1$ spectrum (days)	Periodicity of the leading POP/DMD mode (days)
ERA5	(141.2, 149.7, 152.1)	150.3	147.8
CESM-WACCM	(147.7, 152.3, 161.2)	156.5	149.5
GCM with propagating regime	(139.4, 146.5, 150.7)	146.3	141.8
GCM with non-propagating regime	-	-	-

and their eigenvalues can be complex; as a result, they can be used to identify decaying-oscillatory modes. In fact, Sheshadri and Plumb (2017) showed that in the propagating regime, EOF1 and EOF2 are coupled as the real and imaginary parts, respectively, of a single decaying-oscillatory POP/DMD mode. Figures 2a–d present the leading POP/DMD modes of ERA5 and the idealized GCM with the propagating regime, showing that the real and imaginary parts of each mode closely match EOF1 and EOF2, respectively (see Fig. S3 for a sensitivity analysis). The periods associated with these modes (from the eigenvalues’ imaginary parts), as well the leading POP/DMD modes of the the three other reanalysis products and CESM-WACCM simulations are around 150 days (see Tables 1 and S1). In contrast to all these models/data, which have propagating annular modes, in the idealized GCM with the non-propagating regime, there is no single POP/DMD mode that contains both EOF1 and EOF2. Rather, EOF1 and EOF2 are each the real part of a different real POP/DMD mode (Figs. 2e, f). These modes are exponentially decaying and have no periodicity, consistent with the red spectrum of  $z_1$  in this model (Fig. 1d and Fig. S3c).

The findings from examining the  $z_1$  spectra and the leading POP/DMD modes consistently point to the existence of a  $\sim 150$ -day periodicity in the SAM and in the annular modes of comprehensive and idealized GCMs. Next, we investigate whether this periodicity affects the variability of some of the other key components of the Southern Hemisphere climate (Section 3.2), followed by investigating the source of this periodicity (Section 3.3) and analyzing CMIP models based on a new metric inspired by these findings (Section 4).

## 3.2 Footprints of the SAM's 150-day Periodicity in Precipitation and Surface Wind Stress

The influence of the periodic (and propagating) behavior of the SAM can be seen in the precipitation and surface wind stress across much of the Southern Hemisphere. Figures 3a, 3e, and 3i show the power spectra of the averaged total precipitation from 20°S–80°S and zonal and meridional ocean surface wind stresses from reanalysis datasets. These spectra, particularly those for wind stresses, have prominent, isolated peaks at ~150 days, consistent with the SAM's periodicity. The remaining panels provide further evidence for the influence of the propagating, periodic SAM on these fields by presenting lagged composite plots (see Appendix B for details). As shown in Fig. 3b, at a lag of –75 days, there is a nearly annular band of positive (negative) precipitation anomalies around 30°S (45°S). The positive anomalies then migrate poleward to 45°S and a new band of negative anomalies emerges at 30°S when the lag is equal to 0 (Fig. 3c). The anomaly patterns at a lag of 0 are completely out of phase with those at a lag of –75 days, indicating the first half of the oscillation period. At a lag of 75 days, the annular bands have moved further poleward and now resemble the patterns at a lag of –75 days, thus completing a 150-day cycle (Fig. 3d).

Figures 3f–h and 3j–l show similar, even clearer, propagating 150-day periodic behavior in lagged composite plots of zonal and meridional wind stresses. This is consistent with previous studies demonstrating the influence of the SAM on Southern Ocean surface winds (A. G. Marshall et al., 2018; Hell et al., 2021). Recently, Xue et al. (2021) showed evidence of the coupling between the subseasonal oscillations in the Southern Hemisphere midlatitude ocean and atmosphere. In particular, they found a slower oceanic oscillation on a timescale of ~100–150 days that seems to be forced from the atmosphere. Although we do not further investigate the source of this oceanic oscillation here, we suggest the possibility that it is driven by the propagating SAM on a timescale of ~150 days, given the strong effects of the SAM on Southern Ocean surface winds (A. G. Marshall et al., 2018; Hell et al., 2021).

Overall, the results of Fig. 3 signify the influence of the propagating and 150-day periodic behavior of the SAM on the Southern Hemisphere climate at the hemispheric scale.

## 3.3 Source of the Periodicity: The Propagating Regime of the SAM

The results so far indicate that the power spectra in four reanalysis datasets, CESM-WACCM, and the idealized GCM with a propagating regime have a noticeable peak at around 150 days, matching the periodicity of the leading POP/DMD modes (Figs. 1–2 and Tables 1 and S1). This periodicity also has a clear signature in the variability of the hemispheric-scale precipitation and surface wind stress (Fig. 3).

Below, we show that the source of this periodicity is the propagating regime of the annular modes, and that its underlying dynamics is the cross-EOF eddy feedbacks. In what follows, we first discuss the key characteristics of propagating and non-propagating regimes. Then we present the predictive reduced-order model of Lubis and Hassanzadeh (2021), which provides further insight into the source of this periodicity.

### 3.3.1 Characteristics of Propagating Annular Modes

Figures 4a, b show the patterns of EOF1 and EOF2 as well as the climatological zonal-mean zonal wind in the Southern Hemisphere in the year-round ERA5 reanalysis. Figure 4c presents the one-point lag-correlation map of the zonal-mean zonal wind anomalies integrated across the depth of the troposphere and reconstructed from projections onto EOF1 and EOF2. This map shows that the wind anomalies typically emerge in low latitudes and propagate coherently poleward. This propagating behavior can also



be seen in Fig. 4d, which presents the cross-correlation between  $z_1$  and  $z_2$  (the PCs of EOF1 and EOF2) at different time lags. While PCs are independent at a lag of 0 by design,  $z_1$  and  $z_2$  are rather strongly correlated at large positive and negative time lags ( $> \pm 7$  days), peaking at around  $\pm 10$  days. This suggests that after about 7 days, the EOF2 (EOF1) pattern drifts poleward and resembles that of EOF1 (EOF2, but with the opposite sign).

To better demonstrate the distinction between the annular mode's propagating and non-propagating behavior (loosely called regimes), Figs. 5a–c show the one-point lag-correlation maps and  $z_1 z_2$  cross-correlations for two specific setups of an idealized GCM (a dry dynamical core). Figure 5a shows that in one setup (the original Held-Suarez setup (Held & Suarez, 1994)), the anomalies emerge and decay in the same latitude bands and do not meridionally propagate. In this non-propagating regime, the annular mode is very persistent, and as seen in Fig. 5c,  $z_1$  and  $z_2$  have small (often statistically insignificant) cross-correlations at any time lag. In contrast, the annular mode of the other setup is in the propagating regime: the anomalies propagate meridionally (Fig. 5b), and  $z_1$  and  $z_2$  have strong cross-correlations that peak at around  $\pm 20$  days (Fig. 5c).

As discussed in earlier studies (Son & Lee, 2006; Son et al., 2008; Sparrow et al., 2009; Sheshadri & Plumb, 2017; Lubis & Hassanzadeh, 2021; I. N. James & Dodd, 1996) and as shown in Figs. 4c, d and 5a–c, the propagating annular mode is characterized by the meridional propagation of the large-scale zonal wind anomalies in the midlatitude troposphere, in which the variability is dominated not by EOF1 alone, but by coupled EOF1 and EOF2. The existence of the propagating regime in the Southern Hemisphere is evident from the one-point lag-correlation map in Fig. 4c and the  $z_1 z_2$  cross-correlation in Fig. 4d, although the poleward-propagating signal and the cross-correlations are not as strong as those in the idealized GCM (Figs. 5b, c; also see Sheshadri and Plumb (2017)). Recently, Lubis and Hassanzadeh (2021) showed that this EOF1-EOF2 coupling has important implications for eddy-zonal flow interactions in the annular mode dynamics and the reduced-order model needed to describe the Southern Hemisphere large-scale zonal-mean circulation, as briefly discussed below.

Figure 4e shows the cross-correlation between  $z_j$  and  $m_j$  at different time lags for  $j = 1$  and 2 in the Southern Hemisphere, where  $m_j$  is the time-series of the eddy momentum forcing on the  $j$ th EOF and is computed as the eddy momentum flux divergence regressed onto  $z_j$  (see Eq. (2) and Supporting Information). As discussed by Lorenz and Hartmann (2001) and in many later studies, the positive  $m_1 z_1$  cross-correlations at positive time lags of 4–20 days indicate an EOF1-onto-EOF1 positive feedback through eddy-mean flow interaction: the anomalous zonal-mean flow associated with EOF1 modifies the transient eddies at timescales longer than synoptic timescales such that these eddies reinforce EOF1, thus increasing the annular mode's persistence (Simpson et al., 2013a; Byrne et al., 2016; Ma et al., 2017; Hassanzadeh & Kuang, 2019). The LH01 reduced-order model, which is explained shortly, describes the variability of EOF1 alone and accounts for this positive EOF1-onto-EOF1 feedback. Unlike EOF1,  $m_2 z_2$  cross-correlations are negligible beyond +5 days, indicating that there is no EOF2-onto-EOF2 feedback. Figure 5d shows similar behavior in both propagating and non-propagating regimes in the two setups of the idealized GCM: positive (negligible)  $m_1 z_1$  ( $m_2 z_2$ ) cross-correlations occur at time lags beyond +5 days.

Given the coupling of EOF1 and EOF2 at time lags of 4–20 days in the propagating regime, Lubis and Hassanzadeh (2021) proposed that in addition to EOF1-onto-EOF1 feedback, there might be also cross-EOF feedbacks: EOF1 (EOF2) may affect EOF2 (EOF1) by modifying  $m_2$  ( $m_1$ ). Figure 4f shows that  $m_1$  and  $z_2$  and  $m_2$  and  $z_1$  indeed have relatively strong positive and negative correlations, respectively, beyond the synoptic timescales, suggesting the existence of cross-EOF feedbacks (note that P. M. James et al. (1994) and Lorenz and Hartmann (2001) also found evidence of a propagating feedback common to both EOF1 and EOF2). Figure 5e further shows that such cross-correlations exist in the

propagating regime but not in the non-propagating regime. Consequently, Lubis and Hassan-zadeh (2021) proposed an extension to the LH01 reduced-order model to explicitly account for EOF1-EOF2 coupling and the cross-EOF feedbacks.

### 3.3.2 The Reduced-Order Model for Propagating Annular Modes: A Predictive Model for the Periodicity

Following the approach of Lorenz and Hartmann (Lorenz & Hartmann, 2001), prognostic equations for  $z_1$  and  $z_2$  can be derived by projecting the zonal-mean, vertically averaged zonal momentum equation onto EOF1 and onto EOF2:

$$\frac{dz_1}{dt} = m_1 - \frac{z_1}{\tau_1}, \quad (4)$$

$$\frac{dz_2}{dt} = m_2 - \frac{z_2}{\tau_2}, \quad (5)$$

where  $t$  is time. The last term in each equation represents damping (mainly due to surface friction), which is modeled as Rayleigh drag with a timescale  $\tau$ . Assuming that eddy-zonal flow feedbacks (i.e., the impact of  $z_j$  on  $m_k$ ) can be adequately represented using a linear model and that the eddy forcing  $m_j$  does not have long-term memory independent of the variability in the zonal-mean flow, one can further write  $m_1 = \tilde{m}_1 + b_{11}z_1 + b_{12}z_2$  and  $m_2 = \tilde{m}_2 + b_{21}z_1 + b_{22}z_2$ . Here, the constant  $b_{jk}$  is the strength of the feedback of  $z_k$  onto  $z_j$  through the modification of  $m_j$  ( $b_{12}$  and  $b_{21}$  are the strengths of cross-EOF feedbacks).  $\tilde{m}_j$  is the random eddy forcing, independent of the zonal-mean flow (thus, not a function of any  $z$ ). Note that the above assumptions are the same as those proposed by Lorenz and Hartmann (2001).

Table 2 shows the values of  $b_{jk}$  and  $\tau_j$  estimated from data from ERA5, the two idealized GCM setups, and CESM-WACCM. In ERA5, the idealized GCM with a propagating regime, and CESM-WACCM,  $b_{12}$  and  $b_{21}$  are not small; rather, they are of the same order of magnitude as  $b_{11}$ , indicating the importance of explicitly accounting for the cross-EOF feedbacks. In the idealized GCM with a non-propagating regime,  $b_{12}$  and  $b_{21}$  are much smaller than  $b_{11}$  and are nearly zero.

With  $b_{12} = 0$ , Eq. (4) becomes the celebrated single-EOF1 LH01 model, which only admits an exponentially decaying solution with a damping timescale  $(b_{11} - 1/\tau_1)$ . However, depending on the six values of  $b_{jk}$  and  $\tau_j$ , the coupled EOF1-EOF2 model of Eqs. (4) and (5) can have two types of solutions: exponentially decaying solutions, which correspond to the non-propagating regime, or decaying-oscillatory solutions, which correspond to the propagating regime (Lubis & Hassan-zadeh, 2021). In particular, the analytical solution of Eqs. (4) and (5) in the deterministic limit  $\tilde{m}_j = 0$  (see the Supporting Information for the derivation) shows that the necessary and sufficient condition for the existence of the decaying-oscillatory solution is

$$\left\{ \left( \frac{1}{\tau_1} - \frac{1}{\tau_2} \right) - (b_{11} - b_{22}) \right\}^2 + 4b_{12}b_{21} < 0, \quad (6)$$

which also indicates that a necessary condition is  $b_{12}b_{21} < 0$ , i.e., non-zero cross-EOF feedbacks of opposite signs. Equation (6) correctly predicts the regime of ERA5, the idealized GCMs, and CESM-WACCM based on the estimated  $b_{jk}$  and  $\tau_j$  values; see Table 2. More importantly, the analytical solution also shows that the frequency of this oscillation (propagation) is

$$\omega = \frac{1}{2} \sqrt{\left\{ \left( \frac{1}{\tau_1} - \frac{1}{\tau_2} \right) - (b_{11} - b_{22}) \right\}^2 + 4b_{12}b_{21}}. \quad (7)$$

Inserting the estimated  $b_{jk}$  and  $\tau_j$  values for ERA5 (Table 2), MERRA2, NCEP1, or NCEP2 into Eq. (7) leads to the prediction that the SAM oscillates with a period of

**Table 2.** Feedback strengths and damping timescales estimated from data from the ERA5 reanalysis, two idealized GCM setups, and CESM-WACCM. The feedback strengths  $b_{jk}$  and damping timescales  $\tau_j$ ,  $i, k = 1, 2$ , appear in the coupled EOF1-EOF2 reduced-order model (see Eqs. (4) and (5)). Values of  $b_{jk}$  are estimated (in  $\text{day}^{-1}$ ) from data using the method introduced in Lubis and Hassanzadeh (2021), which is based on the lagged-regression method of Simpson et al. (2013a); see the Supporting Information for details. Values of  $\tau_j$  are estimated (in  $\text{day}^{-1}$ ) using the method outlined in Lorenz and Hartmann (2001). Values of  $b_{jk}$  are reported as the mean and the 25th and 75th percentiles of the estimated feedback value distribution (calculated over the range of the time lag  $\ell$  shown in the next-to-last column; see the Supporting Information for details). The 25th and 75th percentiles provide a measure of the uncertainty with respect to the choice of the lag time  $\ell$ . The last column indicates whether the annular mode is in the propagating or non-propagating regime according to the theoretically derived criterion (Eq. (6)) given these estimates of  $b_{jk}$  and  $\tau_j$ .

Data	Feedbacks ( $\text{day}^{-1}$ ) (25 <sup>th</sup> , mean, 75 <sup>th</sup> )				$\tau_1$	$\tau_2$	Time lags $\ell$ (days)	Predicted regime based on Eq. (6)
	$b_{11}$	$b_{12}$	$b_{21}$	$b_{22}$				
ERA5	(0.0451, 0.0475, 0.0489)	(0.0697, 0.0714, 0.0719)	(-0.0317, -0.0283, -0.0276)	(0.0133, 0.0137, 0.0140)	8.3	8.4	7–15	propagating
CESM- WACCM	(0.0435, 0.0445, 0.0551)	(0.0650, 0.0658, 0.0667)	(-0.0317, -0.0293, -0.0290)	(0.0103, 0.0127, 0.0129)	8.2	8.3	7–15	propagating
GCM with propagating regime	(0.0921, 0.0937, 0.1074)	(0.0631, 0.0647, 0.0805)	(-0.0465, -0.0430, -0.0382)	(0.0285, 0.0287, 0.0307)	7.4	7.6	8–20	propagating
GCM with non-propagating regime	(0.1231, 0.1247, 0.1275)	(0.0029, 0.0030, 0.0031)	(0.0017, 0.0018, 0.0020)	(0.0155, 0.0175, 0.0185)	7.1	7.4	8–20	non-propagating

~ 150 days, which is basically the same as the period identified by the peak of the power spectra and the eigenvalue of the leading the leading POP/DMD mode (Tables 1 and S1; Figs. 1 and S2). Similarly, based on the estimated  $b_{jk}$  and  $\tau_j$  values (Table 2), Eq. (7) predicts periods of about 146.5 and 152.3 days for the annular modes of the idealized GCM with a propagating regime and CESM-WACCM, respectively (Table 1), consistent with the results from the power spectra and POP/DMD analysis (Fig. 1 and Table 1). In contrast, the circulation of the idealized GCM with a non-propagating regime does not satisfy Eq. (6), simply because  $b_{12}b_{21} > 0$  (Table 2). Therefore, the reduced-order model correctly predicts the existence of the non-propagating regime, and lack of any periodicity in the power spectra of POP/DMD modes of this GCM, consistent with the results of Figs. 1–2.

To further demonstrate the distinction between the  $z_1$  power spectra of propagating and non-propagating annular modes, we also conduct a number of experiments using a stochastic prototype of Eqs. (4)–(5). In these experiments, a range of values of eddy feedbacks and damping are prescribed to produce propagating and non-propagating regimes (see the Supporting Information and Table S2 for details). Figure S4 shows the power spectra of the synthetic data from these experiments. In the non-propagating regime, the power spectrum is red and has no periodicity (black curve in Fig. S4); it closely resembles the one in Fig. 1d. However, in the propagating regime, the spectrum has a peak

(red curve in Fig. S4), exactly as predicted from the reduced-order model, that resembles the one in Fig. 1c. It is also demonstrated that the stronger the cross-EOF eddy feedbacks, the shorter the periodicity (green and orange curves in Fig. S4), suggesting the importance of these feedbacks in setting the oscillatory behavior and persistence of the SAM (shorter periodicity leads to shorter persistence (Lubis & Hassanzadeh, 2021); see below).

These results show the ability of the coupled EOF1-EOF2 reduced-order model (Eqs. (4)–(5)) to predict the  $\sim 150$ -day periodicity of the extratropical, large-scale circulation when the only source of variability is the internal dynamics of the atmosphere, as is the case in the idealized GCMs. Even in the reanalysis and a fully coupled GCM (CESM-WACCM), where there are additional sources of variability, the periodicity predicted by Eq. (7) is robustly detectable in the power spectra and the leading POP/DMD modes. These results also demonstrate that the source of the periodicity is the annular mode’s propagating regime, which itself is tied to the existence of non-zero cross-EOF eddy feedbacks.

#### 4 Implications for the Persistence of the SAM in CMIP Models: A New Metric

Most GCMs, from idealized models to the state-of-the-art CMIP models, simulate annular modes that are too persistent, i.e., the  $e$ -folding decorrelation time of  $z_1$  is too large compared to that of a reanalysis (Simpson & Polvani, 2016; J. Lee et al., 2021; Gerber, Voronin, & Polvani, 2008). This has caused some concerns about the fidelity of these models in simulating the large-scale circulation’s response to increased greenhouse gas concentrations (Simpson & Polvani, 2016; Gerber, Voronin, & Polvani, 2008; Gerber, Polvani, & Ancukiewicz, 2008; Hassanzadeh & Kuang, 2016), particularly as the problems has persisted through phase 3 to 6 of CMIP (Bracegirdle et al., 2020; Simpson et al., 2020; Morgenstern, 2021; J. Lee et al., 2021). Figure 6 shows the autocorrelation function of  $z_1$  in the period of 1960–2005 in a number of CMIP5 (Taylor et al., 2012) and CMIP6 (Eyring et al., 2016) models. In general, CMIP6 models show a significant improvement in the representation of the SAM timescale year-round: in CMIP5 models, the  $e$ -folding decorrelation time is  $15.5 \pm 4.5$  days, while it is  $12.4 \pm 1.7$  days in CMIP6 models, which is closer to the 11.3 days timescale of ERA5. This improvement in the SAM timescales of the CMIP6 models can also be seen from the spread of the autocorrelation functions, which is much narrower compared to CMIP5 models (Figs. 6a, c).

Recent studies have reported that improved SAM timescales in CMIP6 is related to a reduced equatorward bias in the jet latitude (Bracegirdle et al., 2020). However, the underlying physics that control the timescale of the SAM, and even annular modes in idealized models, remain unclear, making it difficult to pinpoint the source(s) of improvement and to devise strategies for further reducing the bias (Nie et al., 2014; Byrne et al., 2016; Hassanzadeh & Kuang, 2019). The reduced-order model (Eqs. (4)–(5)) suggests that the overly persistent annular modes in GCMs can be attributed to a too-strong EOF1-onto-EOF1 positive feedback, i.e., a too-large  $b_{11}$  (Chen & Plumb, 2009; Hassanzadeh & Kuang, 2016). For example,  $b_{11}$  in the idealized GCM with the non-propagating regime is 2.6 times larger than it is in ERA5 (Table 2), and the annular mode in this GCM is 5.6 times more persistent ( $e$ -folding decorrelation time of 11.3 days versus 64.5 days). Until recently, this was believed to be the reason for the too-persistent SAM in CMIP models. However, as shown in Sheshadri and Plumb (2017) and firmly demonstrated in Lubis and Hassanzadeh (2021), for propagating annular modes, the  $e$ -folding decorrelation time depends not only on the decay rate but also on the period of the decaying-oscillatory mode, and the latter is a function of all four feedback amplitudes (Eq. (7)). In fact, increasing the period increases the decorrelation time and thus the persistence (Lubis & Hassanzadeh, 2021). For example, the idealized GCM with a propagating regime has a  $b_{11}$  value that is comparable to that of the GCM with a non-propagating regime (just 25% smaller; see Table 2); however, the decorrelation time in this setup is compa-

465 rable to that of the reanalysis (14.1 days versus 11.3 days). The implication of these re-  
 466 sults is that overly persistent annular modes might be partially (if not entirely) due to  
 467 a periodicity that is too long, for example, because of small cross-EOF feedbacks or even  
 468 the total absence of the propagating regime. This suggests that GCMs with well-simulated  
 469 propagating regimes will have more realistic annular mode timescales than GCMs with  
 470 weakly or non- propagating regimes.

471 To better understand the connections between the persistence of the SAM and the  
 472 propagating regimes in the CMIP models, we first analyze the  $z_1 z_2$  cross-correlations in  
 473 Figs. 6b, d. The multi-model mean and the spread of the  $z_1 z_2$  cross-correlations indi-  
 474 cate that the propagating regime is better represented by the CMIP6 models compared  
 475 to CMIP5 models. In particular, the  $z_1 z_2$  cross-correlations in many CMIP5 models are  
 476 too small and near zero at positive lags, indicating poorly coupled EOF1 and EOF2, and  
 477 hence, weak or non-existing propagating regimes.

478 To better quantify the effect of the propagating regime and the associated period-  
 479 icity on the SAM persistence, we first compute two measures: 1) the similarity between  
 480 the  $z_1 z_2$  cross-correlation functions from each model and reanalysis data (e.g., ERA5),  
 481 and 2) the periodicity of the SAM in each model. For (1), we compute the pattern cor-  
 482 relation ( $r$ ) and the root-mean-square error (RMSE) between  $z_1 z_2$  of each model and ERA5  
 483 for lag times of  $-30$  to  $+30$  days, which represent the period of the maximum cross-correlations  
 484 in ERA5 (see Fig. 6b). We use both  $r$  and RMSE to separately capture the similarity  
 485 in structure and in amplitude of the cross-correlation functions. For (2), we compute  $\lambda_I$ ,  
 486 which as described before, is the imaginary part of the eigenvalue of the POP/DMD mode  
 487 corresponding to the propagating annular mode (see Materials and Methods). We use  
 488  $\lambda_I$ , rather than the peak of the  $z_1$  spectrum, because finding this eigenvalue in the POP/DMD  
 489 analysis is more robust and objective compared to finding the spectral peak.

490 Figures 7a and d show the CMIP5 and CMIP6 models on a  $r$ -RMSE map. We have  
 491 applied a  $k$ -means cluster algorithm (Hartigan & Wong, 1979) to the  $r$  and RMSE val-  
 492 ues and retained only three clusters, representing the high-fidelity (black), medium-fidelity,  
 493 and low-fidelity models. Consistent with the results of Fig. 6b and d, more CMIP6 mod-  
 494 els compared to CMIP5 models are clustered in the region of small (high) RMSE ( $r$ ) val-  
 495 ues, indicating more similarity with the ERA5  $z_1 z_2$  cross-correlation function. Figures 7b  
 496 and e present the decorrelation timescale of  $z_1$  (the commonly used metric for SAM's  
 497 persistence (Gerber, Voronin, & Polvani, 2008; Gerber, Polvani, & Ancukiewicz, 2008))  
 498 as a function of  $r$ , demonstrating that SAM's persistence is better represented in mod-  
 499 els with higher  $r$  (the relationship is more evident in CMIP5 models). Figures 7c and  
 500 f further show, clearly, that models with too-persistent SAM (and low  $r$ , high RMSE)  
 501 in fact have periodicities that are too long. Considered all together, these results are con-  
 502 sistent with the solution of the reduced-order model (Eq. 7), which indicates that overly  
 503 persistent annular modes might be partially (if not entirely) due to a periodicity that  
 504 is too long.

505 Based on these findings, we argue that capturing the propagating regime of SAM  
 506 and its periodicity should be considered as a part of CMIP model evaluations, and that  
 507 such analysis can potentially reveal the source(s) of model biases and lead to improve-  
 508 ments. We suggest a combination of ( $r$ , RMSE, and  $\lambda_I$ ), which can be easily computed  
 509 from  $z_1$  and  $z_2$ , as a new metric for this purpose, which should be used along with the  
 510 commonly used metric, i.e., the decorrelation time of  $z_1$ .

## 511 5 Summary and Discussion

512 In this study, we show that the Southern Hemisphere large-scale extratropical at-  
 513 mospheric circulation has an intrinsic, ultra-low-frequency oscillation with a period of  
 514  $\sim 150$  days. This periodicity is robustly detectable via two vastly different (and indepen-



dent) methods: one is based on analyzing the power spectrum of the SAM's zonal index and the other is based on analyzing the leading dynamical mode of the daily zonal-mean zonal wind (obtained from a POP/DMD analysis). The 150-day period is firmly consistent with the predictions of a new reduced-order model for propagating annular modes introduced recently by Lubis and Hassanzadeh (2021). The reduced-order model (Eqs. (4) and (5)) and idealized modeling experiments suggest that the periodicity is tied to the existence of a propagating regime in the SAM in which the two leading EOFs of the zonal-mean zonal wind interact and form a decaying-oscillatory mode of variability. The timescale of this periodic oscillation depends on the strengths of the feedbacks that these two EOFs exert on themselves and on each other by modifying the eddy momentum fluxes at the shorter timescales of 10–20 days. As such, unlike many other periodic oscillations in the climate system that are externally generated by astronomical/orbital forcing, this periodicity is internally generated. The idealized GCM experiments (with a dry dynamical core) show unambiguously that the periodicity is intrinsic to the extratropical atmosphere, i.e., it arises from the extratropical troposphere's internal dynamics and exists in the absence of ocean and tropical variabilities (including QBO and ENSO) and the seasonal cycle. Note that while here we show the propagating annular mode (and periodicity) in one specific setup of the dry dynamical core, there are various setups of this idealized GCM that produce the propagating regime (Son & Lee, 2006; Sheshadri & Plumb, 2017). Examining some of these setups shows that, unsurprisingly, the propagating regimes of some mean states might have periods other than 150 days, such as, for example, 170 days, though they are always consistent with the predictions of Eq. (7).

This periodicity in the SAM is only the second example of periodicity arising from the internal dynamics of the extratropical large-scale atmospheric circulation, whose turbulent nature favors chaotic rather than periodic (and ordered) variability. The only other example is the recently discovered BAM (Thompson & Barnes, 2014), which also occurs in the Southern Hemisphere. It should be noted that the 150-day periodicity of the SAM reported here and the 20–30-day periodicity of the BAM not only have different timescales but also have different mechanisms. Unlike the dynamics of the SAM's periodicity described above, the BAM is a result of the interaction between the anomalous baroclinicity and eddy heat flux associated with a single EOF, the leading EOF of the EKE. In general, the BAM and SAM are viewed as independent modes (Thompson & Woodworth, 2014), although a few recent studies have suggested some connections between them (Boljka et al., 2018; Lindgren et al., 2020).

The periodicity reported here is a fundamental component of the Southern Hemisphere large-scale circulation variability and dynamics. Additionally, the periodicity might potentially have important implications for the Southern Hemisphere climate variability and for climate model evaluations. As shown in the current study, footprints of the 150-day periodicity can be clearly detected in the power spectra and composite analyses of the precipitation and ocean surface wind stress. While the 150-day periodicity operates on timescales dominated by the seasonal cycle, it could amplify/suppress the seasonal cycle's influence on Southern Hemisphere oceans and, more broadly, climate variability, given the SAM's well-known influence across a broad range of timescales. Whether such an impact is significant, and how this periodicity might change under anthropogenic climate change, should be studied in future work. It should also be mentioned that in all reanalysis products (and in CESM-WACCM), there is another noticeable peak in the power spectra of  $z_1$  at  $>500$  days (Figs. 1a, b and S1-S2). This peak is likely related to what is discussed by Byrne et al. (2016) and is attributed to the influence of ENSO and QBO on the Southern Hemisphere polar vortex variability; therefore, unlike the  $\sim 150$ -day periodicity, it is not internally generated in the extratropical circulation.

How well the GCMs simulate the spatio-temporal variability of the SAM is often used as a key metric in evaluating their fidelity. The most common metric is the  $e$ -folding decorrelation time of the zonal index ( $z_1$ ), which is a measure of the SAM's temporal



persistence (Gerber, Voronin, & Polvani, 2008). Until now, the well-documented overly persistent SAM (too large decorrelation time) of CMIP models was often attributed to a too-strong EOF1-onto-EOF1 positive feedback. Here, we show strong connections between the SAM’s persistence, and how well the SAM’s propagating regime and the corresponding periodicity are simulated in a model compared to reanalysis (Figs. 6 and 7). These results suggest that a too-weak EOF1-EOF2 cross-feedback is even more likely to be the source of this bias. Building on these findings, we suggest a new metric for further quantitatively evaluating GCMs. Note that calculating the 4 feedback values in CMIP models could be particularly insightful; however, such calculations require subdaily data (Ma et al., 2017), which are currently unavailable for most models.

Finally, a deeper dynamical understanding of propagating annular modes, cross-EOF feedbacks, and the periodicity is needed to improve GCMs and better analyze the Southern Hemisphere climate variability. The reduced-order model (Eqs. (4) and (5)) shows that non-zero cross-EOF eddy feedbacks are necessary for the existence of the propagating regime (Eq. (6)); however, this does not rule out the possibility that the propagating anomalies themselves might be essential for the cross-EOF eddy feedbacks (Lorenz & Hartmann, 2001; Lubis & Hassanzadeh, 2021). Extensive idealized modeling experiments by S. Lee et al. (2007) and Son and Lee (Son & Lee, 2006) suggested that the propagating and non-propagating regimes dominate when the climatological zonal-mean zonal wind has double- and single-jet structures, respectively. Their analysis further pointed to the critical role of the mean potential vorticity meridional distribution and an orchestrated combination of linear Rossby wave propagation, nonlinear wave breaking, and radiative relaxation as the key component of the propagating regime dynamics (also, note that while the periodicity is internally generated in the extratropical troposphere, phenomena such as ENSO and QBO can indirectly influence it by modifying the tropospheric mean state). Further theoretical, observational, and modeling analyses are needed to fully understand how the mean state and other factors determine the four feedback amplitudes in Eqs. (6) and (7), and thus the regime and timescale of the periodicity. In summary, such a deep dynamical understanding, combined with the new metric introduced above, can lead to a better understanding the source(s) of CMIP models’ biases (those related to SAM and its impacts), and potentially improving the GCMs.

## Appendix A Principal Oscillation Pattern (POP) and Dynamic Mode Decomposition (DMD) Analysis

Let’s consider a dynamical system that is exactly or approximately modeled by the linear equation

$$\dot{x} = \mathbf{A}x + \xi, \quad (\text{A1})$$

where  $x(t)$  is the state vector of size  $n$ ,  $\mathbf{A}$  is the dynamical operator ( $n \times n$  matrix), and  $\xi(t)$  represents stochastic noise (a vector of size  $n$ ). If  $\mathbf{A}$  is not known but a large enough number of snapshots of  $x$ , i.e.,  $\{x_1, x_2 \dots x_N\}$ , are available, then  $\mathbf{A}$  (and thus its eigenvectors and eigenvalues) can be approximated. One common approach to finding  $\mathbf{A}$  from climate data is the linear inverse modeling (LIM) method of Penland (Penland, 1989), which uses the solution of the Fokker-Planck equation to Eq. (A1); in this approach, the eigenvectors of  $\mathbf{A}$  are often called principal oscillation patterns (POPs) (Hasselmann, 1988). Another approach, more recently developed in the dynamical systems community based on least-squares regression, is dynamic mode decomposition (DMD) (Schmid, 2010); in this approach, the eigenvectors of  $\mathbf{A}$  are called DMD modes. While the derivations, interpretations, and numerics of LIM and DMD are different, they are in fact mathematically identical (Tu et al., 2014; Khodkar & Hassanzadeh, 2018).

We mention DMD here for two reasons. First, extensive theoretical work in recent years has shown that DMD modes are dynamically relevant even for nonlinear systems, and in fact, under some conditions (including  $N \rightarrow \infty$ ), the DMD modes converge to the nonlinear system’s true dynamical modes, the so-called Koopman modes (Rowley

et al., 2009; Arbabi & Mezić, 2017); see Ghil and Lucarini (2020) for recent work in the context of the climate system. These findings provide further support for the relevance of POP/DMD modes to the analysis of the extratropical circulation, where the underlying dynamics are inherently nonlinear. Second, calculations of the POP/DMD modes from data for high-dimensional nonlinear systems may not be robust when  $N$  is not large enough, as is the case in practice (Sheshadri & Plumb, 2017; Khodkar & Hassanzadeh, 2018; Hassanzadeh & Kuang, 2016). A number of stable numerical algorithms for the robust computation of the POP/DMD modes have been introduced by the dynamical systems community; here, we use the Exact DMD algorithm of Tu et al. (2014).

Suppose that  $x_k$  includes the zonal-mean zonal wind pattern on day  $k$ . The pattern, which is a function of latitude and pressure, is weighted by  $\sqrt{\cos(\phi)}$  and vectorized (size =  $n$ ). Then,  $N$  sequential daily snapshots form matrices  $\mathbf{X}$  and  $\mathbf{Y}$ :

$$\mathbf{X} = [x_1 \ x_2 \ \dots \ x_{N-\theta}], \quad (\text{A2})$$

$$\mathbf{Y} = [x_{1+\theta} \ x_{2+\theta} \ \dots \ x_N], \quad (\text{A3})$$

where  $\theta$  is a chosen time lag (further discussed later). The size of matrices  $\mathbf{X}$  and  $\mathbf{Y}$  is  $n \times (N - \theta)$ . The reduced singular value decomposition (SVD) of matrix  $\mathbf{X}$  leads to

$$\mathbf{X} = \mathbf{U}\Sigma\mathbf{V}^*, \quad (\text{A4})$$

where  $*$  indicates the conjugate transpose. The matrix  $\mathbf{L}(\theta) = \exp(\mathbf{A}\theta)$  is then estimated as

$$\tilde{\mathbf{L}}(\theta) = \mathbf{U}^*\mathbf{Y}\mathbf{V}\Sigma^{-1}, \quad (\text{A5})$$

where  $\tilde{\mathbf{L}} = \mathbf{U}^*\mathbf{L}\mathbf{U}$ . The eigenvectors and eigenvalues of matrix  $\tilde{\mathbf{L}}$  are calculated using eigendecomposition:

$$\tilde{\mathbf{L}}(\theta) = \mathbf{W}\Gamma(\theta)\mathbf{W}^{-1}, \quad (\text{A6})$$

where the diagonal elements of  $\Gamma$  are the eigenvalues of  $\mathbf{L}$ . The columns of  $\mathbf{W}$  are related to the eigenvectors of  $\mathbf{L}$  and  $\mathbf{A}$  via

$$\Phi = \mathbf{U}\mathbf{W}, \quad (\text{A7})$$

where the columns of  $\Phi$  are the POP/DMD modes, i.e., the eigenvectors of  $\mathbf{A}$ . The eigenvalues of  $\mathbf{A}$  are the diagonal elements  $\lambda$  of matrix  $\Lambda$ , which is computed as

$$\Lambda = \frac{1}{\theta} \ln \Gamma. \quad (\text{A8})$$

Unlike EOF modes, which are always real and orthonormal, the POP/DMD modes (and their eigenvalues  $\lambda$ ) can be complex numbers, and in general they are not orthonormal. As a result, the POP/DMD modes can identify decaying as well as decaying-oscillatory modes. In particular,

$$\lambda = \lambda_R \pm i\lambda_I, \quad (\text{A9})$$

where the real part  $\lambda_R$  is the decay rate and the imaginary part  $\lambda_I$  is the frequency of oscillation. It should be noted that while the numerical procedure outlined in Eqs. (A4)–(A8) might seem different from the common LIM algorithm, they are in fact mathematically the same. Both DMD and LIM attempt to compute  $\mathbf{L}(\theta) = \mathbf{Y}\mathbf{X}^\#$ , where  $\#$  is the pseudo-inverse; see Khodkar and Hassanzadeh (Khodkar & Hassanzadeh, 2018) for details.

There are two issues that require further discussion: i) the choice of  $\theta$  and ii) the identification of the “leading” POP/DMD modes. Regarding (i), Figs. S3 and S7 show that the estimated  $\lambda_R$  and  $\lambda_I$  are fairly insensitive to  $\theta$  ( $2\pi/\lambda_I$  is the periodicity reported in Tables 1 and S1). Regarding (ii), although EOFs are naturally ranked based on their explained variances, no such obvious ranking exists for the POP/DMD modes. Here, we

follow the objective approach outlined in Sheshadri and Plumb (2017) in order to identify the leading POP/DMD mode in each dataset. For data in which the annular mode is in the propagating regime, the leading POP/DMD mode is considered to be the mode whose real and imaginary parts have the largest pattern correlation with the combined EOF1 and EOF2. To be clearer, this is done by first vectorizing the real and imaginary parts of each POP/DMD mode, stacking them together, and then calculating the spatial pattern correlation with respect to a vector of stacked EOF1 and EOF2 patterns. The leading POP/DMD mode found in this way for each dataset/GCM is complex-valued and has a pattern correlation of  $> 0.9$  with the EOF1-EOF2 vector. For the idealized GCM in which the annular mode is in the non-propagating regime, such an approach would yield a maximum pattern correlation of just  $\sim 0.5$ , indicating that no POP/DMD mode contains both EOF1 and EOF2. In this case, we choose the two POP/DMD modes whose real parts have the highest pattern correlations with EOF1 and with EOF2, separately. This approach yields pattern correlations of  $> 0.85$  and POP/DMD modes that are real (Figs. 2e, f).

For the results reported in Fig. 2 and Tables 1 and S1, the value of the time lag  $\theta$  used in the calculation of POP/DMD modes (Eqs. (A2) and (A3)) is 11 days for ERA5, 20 days for the idealized GCM with a propagating regime, 60 days for the idealized GCM with a non-propagating regime, 11 days for CESM1 (WACCM), 11 days for MERRA2, 5 days for NCEP1, and 6 days for NCEP2. For each case, this value of  $\theta$  leads to the leading POP/DMD mode with the highest pattern correlation with the coupled EOF1-EOF2 mode. We apply the same procedure to find the periodicity of propagating annular modes in CMIP models (Figs. 7c, f). We choose the two POP/DMD modes whose real and imaginary parts have the highest correlation with the combined EOF1 and EOF2 at lag times  $\theta$  (1–30 days), which is a range of the decorrelation timescales in CMIP models.

## Appendix B Composite Analysis of Precipitation and Surface Wind Stress

The composite analysis in Fig. 3 is performed using the zonal index,  $z_1$ , from ERA5 year-round data from 1979–2020. First,  $z_1$  is band-pass filtered for the period range of 140–160 days, which corresponds to the period around the peak of the  $z_1$  spectrum (Fig. 1), by using a Lanczos filtering technique with 601 weights. Then, the dates at which this band-pass-filtered time-series reaches its local maxima and minima are identified (central dates). The filtering is important for removing other variability that may obscure the signals. Finally, the filtered anomalies at a specific lag time from the central dates corresponding to the maxima are averaged. The lag times used are 0,  $-75$ , and  $+75$  days. Similarly, the anomalies at a specific lag time from the central dates corresponding to the minima are averaged. Figure 3 shows the difference between these composites (the composite corresponding to the maxima minus the one corresponding to the minima). This composite technique has been used by others, e.g., Thiéblemont (Thiéblemont et al., 2015), who created North Atlantic Oscillation (NAO) composites with respect to an 11-year solar signal by applying a quasi-decadal band-pass filter to NAO indices and anomalous fields.

## Open Research

The ERA5 dataset (Hersbach et al., 2020) is publicly available at <https://apps.ecmwf.int/datasets/data/interim-full-daily/>. The MERRA2 dataset (Bosilovich et al., 2015) is publicly available at <https://gmao.gsfc.nasa.gov/reanalysis/MERRA-2/>. The NCEP1 dataset (Kalnay et al., 1996) and the NCEP2 dataset (Kanamitsu et al., 2002) are publicly available at <https://psl.noaa.gov/data/>. The CESM-WACCM used to generate the data is publicly available at <https://www.cesm.ucar.edu/models/cesm/> and the GFDL idealized GCM is publicly available at <https://www.gfdl.noaa>

.gov/\\idealized-spectral-models-quickstart/. The time-series for zonal indices and eddy momentum forcings ( $z$  and  $m$ ) calculated from ERA5 data, the two idealized GCM setups, and CESM-WACCM have been made available via Zenodo (<http://doi.org/10.5281/zenodo.5085479>). The MATLAB and NCL codes for calculating POP/DMD modes are available at <https://github.com/sandrolubis/DMD-HDMD-Annular-Modes>. The NCL codes for feedback calculations have been shared at <https://github.com/sandrolubis/Cross-EOF-Eddy-Feedback-Model>.

## Acknowledgments

We thank Ding Ma and Aditi Sheshadri for insightful discussions and Ebrahim Nabizadeh, Y. Qiang Sun, Hamid Pahlavan, and Da Yang for helpful comments on the manuscript. Funding: This work is supported by National Science Foundation (NSF) Grants AGS-1921413 and AGS-2046309 and the Office of Naval Research (ONR) Young Investigator Award N00014-20-1-2722 to PH. Computational resources were provided by XSEDE (allocation ATM170020), NCAR’s CISL (allocation URIC0004), and the Rice University Center for Research Computing. SL is supported by the U.S. Department of Energy Office of Science Biological and Environmental Research through the Regional and Global Model Analysis program area. The Pacific Northwest National Laboratory (PNNL) is operated for DOE by Battelle Memorial Institute under contract DE-AC05-76RL01830.

## References

- Arbabi, H., & Mezić, I. (2017). Ergodic theory, dynamic mode decomposition, and computation of spectral properties of the koopman operator. *SIAM Journal on Applied Dynamical Systems*, 16(4), 2096-2126. doi: 10.1137/17M1125236
- Banerjee, A., Fyfe, J. C., Polvani, L. M., Waugh, D., & Chang, K.-L. (2020, Mar 01). A pause in southern hemisphere circulation trends due to the Montreal protocol. *Nature*, 579(7800), 544-548. Retrieved from <https://doi.org/10.1038/s41586-020-2120-4> doi: 10.1038/s41586-020-2120-4
- Boljka, L., Shepherd, T. G., & Blackburn, M. (2018, 05). On the coupling between barotropic and baroclinic modes of extratropical atmospheric variability. *Journal of the Atmospheric Sciences*, 75(6), 1853-1871. doi: 10.1175/JAS-D-17-0370.1
- Bosilovich, M. G., Akella, S., Coy, L., Cullather, R., Draper, C., Gelaro, R., ... Suarez, M. (2015). Merra-2: Initial evaluation of the climate. technical report series on global modeling and data assimilation. *Tech. Rep. NASA/2015-104606*, 43, 136. doi: <http://gmao.gsfc.nasa.gov/reanalysis/MERRA-2/docs/104606>
- Bracegirdle, T. J., Holmes, C. R., Hosking, J. S., Marshall, G. J., Osman, M., Patterson, M., & Rackow, T. (2020). Improvements in circumpolar southern hemisphere extratropical atmospheric circulation in CMIP6 compared to CMIP5. *Earth and Space Science*, 7(6), e2019EA001065. doi: 10.1029/2019EA001065
- Byrne, N. J., Shepherd, T. G., Woollings, T., & Plumb, R. A. (2016). Annular modes and apparent eddy feedbacks in the southern hemisphere. *Geophysical Research Letters*, 43(8), 3897-3902. doi: 10.1002/2016GL068851
- Ceppi, P., & Hartmann, D. L. (2015, Jun 01). Connections between clouds, radiation, and midlatitude dynamics: a review. *Current Climate Change Reports*, 1(2), 94-102. doi: 10.1007/s40641-015-0010-x
- Chen, G., & Plumb, R. A. (2009, 12). Quantifying the eddy feedback and the persistence of the zonal index in an idealized atmospheric model. *Journal of the Atmospheric Sciences*, 66(12), 3707-3720. doi: 10.1175/2009JAS3165.1
- Chiang, J. C. H., Tokos, K. S., Lee, S.-Y., & Matsumoto, K. (2018). Contrasting impacts of the south pacific split jet and the southern annular mode modulation on southern ocean circulation and biogeochemistry. *Paleoceanography and Paleoclimatology*, 33(1), 2-20. Retrieved from <https://>

- agupubs.onlinelibrary.wiley.com/doi/abs/10.1002/2017PA003229 doi:  
https://doi.org/10.1002/2017PA003229
- Eyring, V., Bony, S., Meehl, G. A., Senior, C. A., Stevens, B., Stouffer, R. J., &  
Taylor, K. E. (2016). Overview of the coupled model intercomparison project  
phase 6 (cmip6) experimental design and organization. *Geoscientific Model De-*  
*velopment*, 9(5), 1937–1958. Retrieved from [https://gmd.copernicus.org/](https://gmd.copernicus.org/articles/9/1937/2016/)  
[articles/9/1937/2016/](https://gmd.copernicus.org/articles/9/1937/2016/) doi: 10.5194/gmd-9-1937-2016
- Feldstein, S., & Lee, S. (1998, 10). Is the atmospheric zonal index driven by an eddy  
feedback? *Journal of the Atmospheric Sciences*, 55(19), 3077-3086. doi: 10  
.1175/1520-0469(1998)055<3077:ITAZID>2.0.CO;2
- Feldstein, S. B. (1998). An observational study of the intraseasonal poleward  
propagation of zonal mean flow anomalies. *Journal of the Atmospheric*  
*Sciences*, 55(15), 2516 - 2529. doi: 10.1175/1520-0469(1998)055<2516:  
AOSOTI>2.0.CO;2
- Feldstein, S. B. (2000). The timescale, power spectra, and climate noise prop-  
erties of teleconnection patterns. *Journal of Climate*, 13(24), 4430 -  
4440. Retrieved from [https://journals.ametsoc.org/view/journals/](https://journals.ametsoc.org/view/journals/clim/13/24/1520-0442_2000_013_4430_ttpsac_2.0.co_2.xml)  
[clim/13/24/1520-0442\\_2000\\_013\\_4430\\_ttpsac\\_2.0.co\\_2.xml](https://journals.ametsoc.org/view/journals/clim/13/24/1520-0442_2000_013_4430_ttpsac_2.0.co_2.xml) doi:  
10.1175/1520-0442(2000)013<4430:TTPSAC>2.0.CO;2
- Gerber, E. P., Polvani, L. M., & Ancukiewicz, D. (2008). Annular mode time scales  
in the intergovernmental panel on climate change fourth assessment report  
models. *Geophysical Research Letters*, 35(22). doi: 10.1029/2008GL035712
- Gerber, E. P., & Vallis, G. K. (2007, 09). Eddy-zonal flow interactions and the per-  
sistence of the zonal index. *Journal of the Atmospheric Sciences*, 64(9), 3296-  
3311. doi: 10.1175/JAS4006.1
- Gerber, E. P., Voronin, S., & Polvani, L. M. (2008, 04). Testing the annular mode  
autocorrelation time scale in simple atmospheric general circulation models.  
*Monthly Weather Review*, 136(4), 1523-1536. doi: 10.1175/2007MWR2211.1
- Gettelman, A., Mills, M. J., Kinnison, D. E., Garcia, R. R., Smith, A. K., Marsh,  
D. R., ... Randel, W. J. (2019). The whole atmosphere community climate  
model version 6 (WACCM6). *Journal of Geophysical Research: Atmospheres*,  
124(23), 12380-12403. doi: <https://doi.org/10.1029/2019JD030943>
- Ghil, M., & Lucarini, V. (2020, Jul). The physics of climate variability and climate  
change. *Rev. Mod. Phys.*, 92, 035002. doi: 10.1103/RevModPhys.92.035002
- Gillett, N. P., & Fyfe, J. C. (2013). Annular mode changes in the CMIP5 sim-  
ulations. *Geophysical Research Letters*, 40(6), 1189-1193. Retrieved from  
<https://agupubs.onlinelibrary.wiley.com/doi/abs/10.1002/grl.50249>  
doi: <https://doi.org/10.1002/grl.50249>
- Gillett, N. P., Kell, T. D., & Jones, P. D. (2006). Regional climate impacts of the  
southern annular mode. *Geophysical Research Letters*, 33(23). doi: [https://doi](https://doi.org/10.1029/2006GL027721)  
[.org/10.1029/2006GL027721](https://doi.org/10.1029/2006GL027721)
- Hall, A., & Visbeck, M. (2002). Synchronous variability in the southern hemisphere  
atmosphere, sea ice, and ocean resulting from the annular mode. *Journal of*  
*Climate*, 15(21), 3043 - 3057. Retrieved from [https://journals.ametsoc](https://journals.ametsoc.org/view/journals/clim/15/21/1520-0442_2002_015_3043_svitsh_2.0.co_2.xml)  
[.org/view/journals/clim/15/21/1520-0442\\_2002\\_015\\_3043\\_svitsh\\_2.0](https://journals.ametsoc.org/view/journals/clim/15/21/1520-0442_2002_015_3043_svitsh_2.0.co_2.xml)  
[.co\\_2.xml](https://journals.ametsoc.org/view/journals/clim/15/21/1520-0442_2002_015_3043_svitsh_2.0.co_2.xml) doi: 10.1175/1520-0442(2002)015<3043:SVITSH>2.0.CO;2
- Hartigan, J. A., & Wong, M. A. (1979). A k-means clustering algorithm. *Journal of*  
*the Royal Statistical Society: Series C (Applied Statistics)*, 28(1), 100-108. doi:  
<https://doi.org/10.2307/2346830>
- Hartmann, D. L. (2016). Chapter 4 - the energy balance of the surface. In  
D. L. Hartmann (Ed.), *Global physical climatology (second edition)* (Sec-  
ond Edition ed., p. 95-130). Boston: Elsevier. Retrieved from [https://](https://www.sciencedirect.com/science/article/pii/B9780123285317000049)  
[www.sciencedirect.com/science/article/pii/B9780123285317000049](https://www.sciencedirect.com/science/article/pii/B9780123285317000049)  
doi: <https://doi.org/10.1016/B978-0-12-328531-7.00004-9>
- Hassanzadeh, P., & Kuang, Z. (2016). The linear response function of an idealized



- atmosphere. part ii: Implications for the practical use of the fluctuation-dissipation theorem and the role of operator's nonnormality. *Journal of the Atmospheric Sciences*, 73(9), 3441 - 3452. Retrieved from <https://journals.ametsoc.org/view/journals/atasc/73/9/jas-d-16-0099.1.xml> doi: 10.1175/JAS-D-16-0099.1
- Hassanzadeh, P., & Kuang, Z. (2019, 04). Quantifying the annular mode dynamics in an idealized atmosphere. *Journal of the Atmospheric Sciences*, 76(4), 1107-1124. doi: 10.1175/JAS-D-18-0268.1
- Hasselmann, K. (1988). Pips and pops: The reduction of complex dynamical systems using principal interaction and oscillation patterns. *Journal of Geophysical Research: Atmospheres*, 93(D9), 11015-11021. doi: 10.1029/JD093iD09p11015
- Held, I. M., & Suarez, M. J. (1994). A proposal for the intercomparison of the dynamical cores of atmospheric general circulation models. *Bulletin of the American Meteorological Society*, 75(10), 1825 - 1830. Retrieved from [https://journals.ametsoc.org/view/journals/bams/75/10/1520-0477\\_1994\\_075\\_1825\\_apftio\\_2\\_0\\_co\\_2.xml](https://journals.ametsoc.org/view/journals/bams/75/10/1520-0477_1994_075_1825_apftio_2_0_co_2.xml) doi: 10.1175/1520-0477(1994)075<1825:APFTIO>2.0.CO;2
- Hell, M. C., Cornuelle, B. D., Gille, S. T., & Lutsko, N. J. (2021). Time-varying empirical probability densities of southern ocean surface winds: Linking the leading mode to sam and quantifying wind product differences. *Journal of Climate*, 34(13), 5497 - 5522. doi: 10.1175/JCLI-D-20-0629.1
- Hersbach, H., Bell, B., Berrisford, P., Hirahara, S., Horányi, A., Muñoz-Sabater, J., ... Thépaut, J.-N. (2020). The ERA5 global reanalysis. *Quarterly Journal of the Royal Meteorological Society*, 146(730), 1999-2049. doi: <https://doi.org/10.1002/qj.3803>
- James, I. N., & Dodd, J. P. (1996). A mechanism for the low-frequency variability of the mid-latitude troposphere. *Quarterly Journal of the Royal Meteorological Society*, 122(533), 1197-1210. doi: 10.1002/qj.49712253309
- James, P. M., Fraedrich, K., & James, I. N. (1994). Wave-zonal-flow interaction and ultra-low-frequency variability in a simplified global circulation model. *Quarterly Journal of the Royal Meteorological Society*, 120(518), 1045-1067. doi: <https://doi.org/10.1002/qj.49712051812>
- Kalnay, E., Kanamitsu, M., Kistler, R., Collins, W., Deaven, D., Gandin, L., ... Joseph, D. (1996). The ncep/ncar 40-year reanalysis project. *Bulletin of the American Meteorological Society*, 77(3), 437 - 472. doi: 10.1175/1520-0477(1996)077<0437:TNYRP>2.0.CO;2
- Kanamitsu, M., Ebisuzaki, W., Woollen, J., Yang, S.-K., Hnilo, J. J., Fiorino, M., & Potter, G. L. (2002). Ncep-doe amip-ii reanalysis (r-2). *Bulletin of the American Meteorological Society*, 83(11), 1631 - 1644. doi: 10.1175/BAMS-83-11-1631
- Khodkar, M. A., & Hassanzadeh, P. (2018, Aug). Data-driven reduced modelling of turbulent Rayleigh-Bénard convection using DMD-enhanced fluctuation-dissipation theorem. *Journal of Fluid Mechanics*, 852. Retrieved from <http://dx.doi.org/10.1017/jfm.2018.586> doi: 10.1017/jfm.2018.586
- Kidson, J. W. (1988, 12). Interannual variations in the southern hemisphere circulation. *Journal of Climate*, 1(12), 1177-1198. doi: 10.1175/1520-0442(1988)001<1177:IVITSH>2.0.CO;2
- Kushner, P. J., Held, I. M., & Delworth, T. L. (2001). Southern hemisphere atmospheric circulation response to global warming. *Journal of Climate*, 14(10), 2238 - 2249. Retrieved from [https://journals.ametsoc.org/view/journals/clim/14/10/1520-0442\\_2001\\_014\\_0001\\_shacrt\\_2\\_0\\_co\\_2.xml](https://journals.ametsoc.org/view/journals/clim/14/10/1520-0442_2001_014_0001_shacrt_2_0_co_2.xml) doi: 10.1175/1520-0442(2001)014<0001:SHACRT>2.0.CO;2
- Lee, J., Sperber, K. R., Gleckler, P. J., Taylor, K. E., & Bonfils, C. J. W. (2021). Benchmarking performance changes in the simulation of extratropical modes of



- variability across cmip generations. *Journal of Climate*, 34(17), 6945 - 6969. Retrieved from <https://journals.ametsoc.org/view/journals/clim/34/17/JCLI-D-20-0832.1.xml> doi: 10.1175/JCLI-D-20-0832.1
- Lee, S., Son, S.-W., Grise, K., & Feldstein, S. B. (2007, 03). A mechanism for the poleward propagation of zonal mean flow anomalies. *Journal of the Atmospheric Sciences*, 64(3), 849-868. doi: 10.1175/JAS3861.1
- Limpasuvan, V., Richter, J. H., Orsolini, Y. J., Stordal, F., & Kvissel, O.-K. (2012). The roles of planetary and gravity waves during a major stratospheric sudden warming as characterized in WACCM. *Journal of Atmospheric and Solar-Terrestrial Physics*, 78, 84-98.
- Lindgren, E. A., Sheshadri, A., & Plumb, R. A. (2020). Frequency-dependent behavior of zonal jet variability. *Geophysical Research Letters*, 47(6), e2019GL086585. doi: 10.1029/2019GL086585
- Lorenz, D. J., & Hartmann, D. L. (2001, 11). Eddy-zonal flow feedback in the Southern Hemisphere. *Journal of the Atmospheric Sciences*, 58(21), 3312-3327. doi: 10.1175/1520-0469(2001)058<3312:EZFFIT>2.0.CO;2
- Lubis, S. W., & Hassanzadeh, P. (2021). An eddy-zonal flow feedback model for propagating annular modes. *Journal of the Atmospheric Sciences*, 78(1), 249 - 267. Retrieved from <https://journals.ametsoc.org/view/journals/atsc/78/1/jas-d-20-0214.1.xml> doi: 10.1175/JAS-D-20-0214.1
- Lutsko, N. J., & Hell, M. C. (2021). Moisture and the persistence of annular modes. *Journal of the Atmospheric Sciences*, 78(12), 3951 - 3964. doi: 10.1175/JAS-D-21-0055.1
- Ma, D., Hassanzadeh, P., & Kuang, Z. (2017, 01). Quantifying the Eddy-Jet Feedback Strength of the Annular Mode in an Idealized GCM and Reanalysis Data. *Journal of the Atmospheric Sciences*, 74(2), 393-407. doi: 10.1175/JAS-D-16-0157.1
- Marshall, A. G., Hemer, M. A., Hendon, H. H., & McInnes, K. L. (2018). Southern annular mode impacts on global ocean surface waves. *Ocean Modelling*, 129, 58-74. doi: <https://doi.org/10.1016/j.ocemod.2018.07.007>
- Marshall, G. J. (2003). Trends in the southern annular mode from observations and reanalyses. *Journal of Climate*, 16(24). doi: 10.1175/1520-0442(2003)016<4134:TITSAM>2.0.CO;2
- Mitchell, J. (1976). An overview of climatic variability and its causal mechanisms. *Quaternary Research*, 6(4), 481-493. Retrieved from <https://www.sciencedirect.com/science/article/pii/0033589476900211> doi: [https://doi.org/10.1016/0033-5894\(76\)90021-1](https://doi.org/10.1016/0033-5894(76)90021-1)
- Morgenstern, O. (2021). The southern annular mode in 6th coupled model inter-comparison project models. *Journal of Geophysical Research: Atmospheres*, 126(5), e2020JD034161. Retrieved from <https://agupubs.onlinelibrary.wiley.com/doi/abs/10.1029/2020JD034161> (e2020JD034161 2020JD034161) doi: <https://doi.org/10.1029/2020JD034161>
- Nie, Y., Zhang, Y., Chen, G., Yang, X.-Q., & Burrows, D. A. (2014). Quantifying barotropic and baroclinic eddy feedbacks in the persistence of the southern annular mode. *Geophysical Research Letters*, 41(23), 8636-8644. doi: 10.1002/2014GL062210
- Penland, C. (1989, 10). Random forcing and forecasting using principal oscillation pattern Analysis. *Monthly Weather Review*, 117(10), 2165-2185. doi: 10.1175/1520-0493(1989)117<2165:RFAFUP>2.0.CO;2
- Riehl, H., Yeh, T. C., & seur, N. E. L. (1950). A study of variations of the general circulation. *Journal of Atmospheric Sciences*, 7(3), 181 - 194. doi: 10.1175/1520-0469(1950)007<0181:ASOVOT>2.0.CO;2
- Robinson, W. A. (1991). The dynamics of the zonal index in a simple model of the atmosphere. *Tellus A*, 43(5), 295-305. doi: 10.1034/j.1600-0870.1991.t01-4-00005.x

- Robinson, W. A. (2000, 02). A baroclinic mechanism for the eddy feedback on the zonal index. *Journal of the Atmospheric Sciences*, 57(3), 415-422. doi: 10.1175/1520-0469(2000)057<0415:ABMFTE>2.0.CO;2
- Rowley, C. W., Mezic, I., Bagheri, S., Schallatter, P., & Henningson, D. S. (2009). Spectral analysis of nonlinear flows. *Journal of Fluid Mechanics*, 641, 115-127. doi: 10.1017/S0022112009992059
- Schmid, P. J. (2010). Dynamic mode decomposition of numerical and experimental data. *Journal of Fluid Mechanics*, 656, 5-28. doi: 10.1017/S0022112010001217
- Sheshadri, A., & Plumb, R. A. (2017, 04). Propagating annular modes: empirical orthogonal functions, principal oscillation patterns, and time scales. *Journal of the Atmospheric Sciences*, 74(5), 1345-1361. doi: 10.1175/JAS-D-16-0291.1
- Simpson, I. R., Bacmeister, J., Neale, R. B., Hannay, C., Gettelman, A., Garcia, R. R., ... Richter, J. H. (2020). An evaluation of the large-scale atmospheric circulation and its variability in CESM2 and other CMIP models. *Journal of Geophysical Research: Atmospheres*, 125(13), e2020JD032835. Retrieved from <https://agupubs.onlinelibrary.wiley.com/doi/abs/10.1029/2020JD032835> (e2020JD032835 10.1029/2020JD032835) doi: <https://doi.org/10.1029/2020JD032835>
- Simpson, I. R., & Polvani, L. M. (2016). Revisiting the relationship between jet position, forced response, and annular mode variability in the southern midlatitudes. *Geophysical Research Letters*, 43(6), 2896-2903. Retrieved from <https://agupubs.onlinelibrary.wiley.com/doi/abs/10.1002/2016GL067989> doi: <https://doi.org/10.1002/2016GL067989>
- Simpson, I. R., Shepherd, T. G., Hitchcock, P., & Scinocca, J. F. (2013a). Southern annular mode dynamics in observations and models. part ii: Eddy feedbacks. *Journal of Climate*, 26(14), 5220 - 5241. Retrieved from <https://journals.ametsoc.org/view/journals/clim/26/14/jcli-d-12-00495.1.xml> doi: 10.1175/JCLI-D-12-00495.1
- Simpson, I. R., Shepherd, T. G., Hitchcock, P., & Scinocca, J. F. (2013b, 07). Southern annular mode dynamics in observations and models. Part II: Eddy feedbacks. *Journal of Climate*, 26(14), 5220-5241. doi: 10.1175/JCLI-D-12-00495.1
- Son, S.-W., & Lee, S. (2006, 05). Preferred Modes of Variability and Their Relationship with Climate Change. *Journal of Climate*, 19(10), 2063-2075. doi: 10.1175/JCLI3705.1
- Son, S.-W., Lee, S., Feldstein, S. B., & Ten Hoeve, J. E. (2008, 03). Time scale and feedback of zonal-mean-flow variability. *Journal of the Atmospheric Sciences*, 65(3), 935-952. doi: 10.1175/2007JAS2380.1
- Sparrow, S., Blackburn, M., & Haigh, J. D. (2009, 10). Annular Variability and Eddy-Zonal Flow Interactions in a Simplified Atmospheric GCM. Part I: Characterization of High- and Low-Frequency Behavior. *Journal of the Atmospheric Sciences*, 66(10), 3075-3094.
- Taylor, K. E., Stouffer, R. J., & Meehl, G. A. (2012). An overview of cmip5 and the experiment design. *Bulletin of the American Meteorological Society*, 93(4), 485 - 498. doi: 10.1175/BAMS-D-11-00094.1
- Thiéblemont, R., Matthes, K., Omrani, N.-E., Kodera, K., & Hansen, F. (2015, Sep 15). Solar forcing synchronizes decadal north atlantic climate variability. *Nature Communications*, 6(1), 8268.
- Thompson, D. W. J., & Barnes, E. A. (2014). Periodic variability in the large-scale southern hemisphere atmospheric circulation. *Science*, 343(6171), 641-645. doi: 10.1126/science.1247660
- Thompson, D. W. J., & Solomon, S. (2002). Interpretation of recent southern hemisphere climate change. *Science*, 296(5569), 895-899. doi: 10.1126/science.1069270

- 961 Thompson, D. W. J., & Woodworth, J. D. (2014, 03). Barotropic and baroclinic an-  
962 nular variability in the Southern Hemisphere. *Journal of the Atmospheric Sci-*  
963 *ences*, 71(4), 1480-1493. doi: 10.1175/JAS-D-13-0185.1
- 964 Tu, J. H., Rowley, C. W., Luchtenburg, D. M., Brunton, S. L., & Kutz, J. N. (2014).  
965 On dynamic mode decomposition: Theory and applications. *Journal of Com-*  
966 *putational Dynamics*, 1(2), 391-421.
- 967 Xue, D., Lu, J., Qian, Y., & Zhang, Y. (2021). Evidence for coupling between  
968 the subseasonal oscillations in the southern hemisphere midlatitude ocean  
969 and atmosphere. *Journal of Geophysical Research: Atmospheres*, 126(4),  
970 e2020JD033872. doi: <https://doi.org/10.1029/2020JD033872>

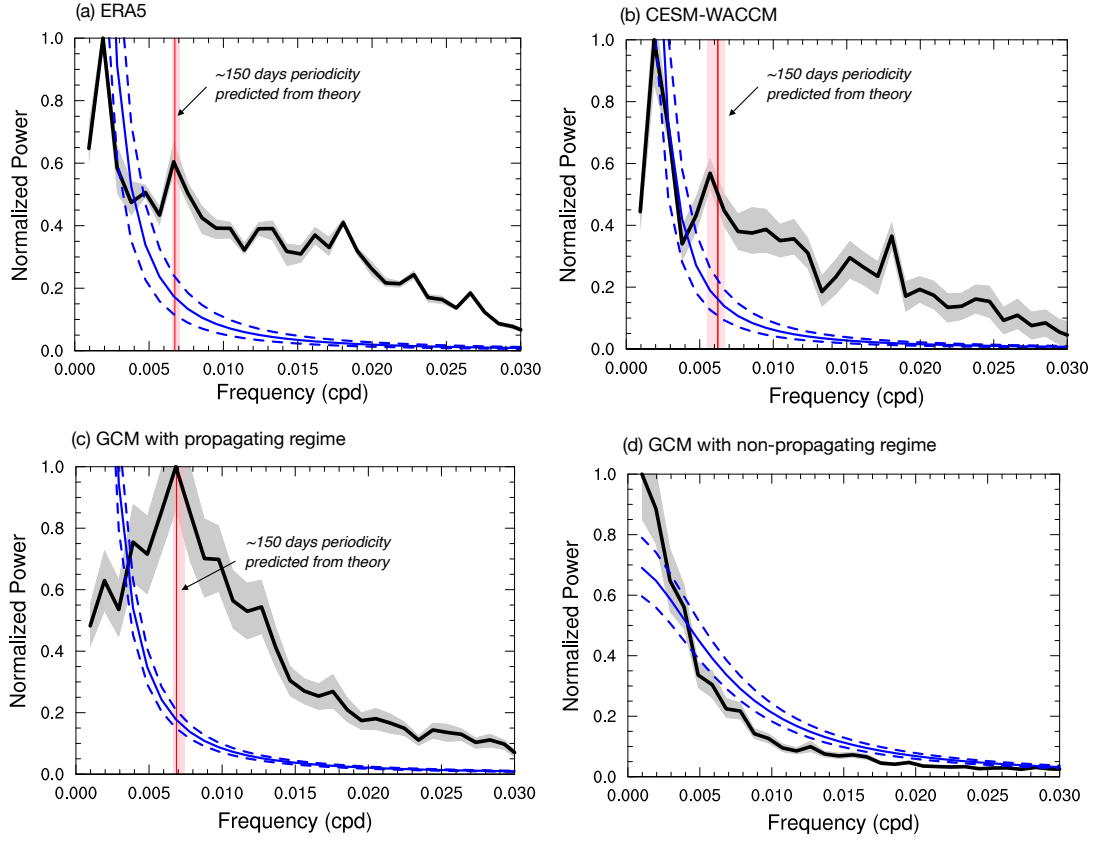


**Figure 1.** Periodicity of the Southern Annular Mode (SAM) in reanalysis data, a fully coupled Earth system model (CESM-WACCM), and two idealized GCM setups. Solid black lines show the normalized power spectra of the Southern Hemisphere zonal index  $z_1$  in (a) ERA5 (1979–2020 year-round), (b) CESM-WACCM, (c) an idealized GCM with a propagating regime, and (d) an idealized GCM with a non-propagating regime. Note that  $z_1$  is computed from seasonal cycle-removed data (see Materials and Methods). The grey shading represents the standard error of the mean: it was computed as the 5% and 95% confidence intervals of the bootstrapped distribution across trials. The red-noise spectra are indicated by the solid blue lines, and the dashed blue lines are the 5% and 95% a priori confidence limits. In panels (a) to (c), the vertical red line and the shading around it show the mean and 25th to 75th percentiles of the theoretically predicted frequency distribution from Eq. (7); the mean period is  $\sim 150$  days (see Table 1 for details). For all cases shown in this figure, except for panel (d), the criterion for the existence of the propagating annular mode (Eq. (6)) is satisfied and Eq. (7) accurately predicts the periodicity. See Materials and Methods and the Supporting Information for more details about the reanalysis data, idealized GCM setups, CESM-WACCM simulation, and spectral analysis of the time-series (including the bootstrapping). Figure S1 shows panel (a) but for different time periods and choices of parameters in spectral analysis. Figure S2 shows the same analysis but for three other reanalysis products.

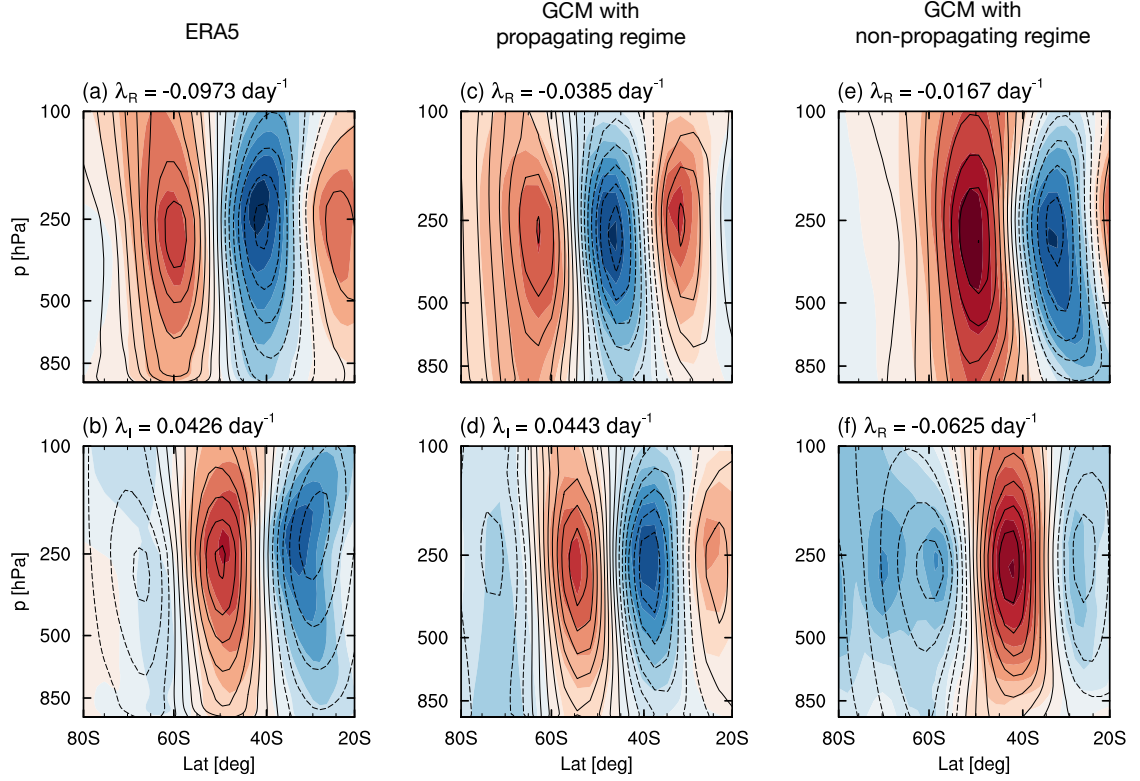


**Figure 2.** Periodicity in the dynamical modes of the zonal-mean Southern Hemisphere extratropical large-scale circulation. Shading shows the (a) real and (b) imaginary parts of the leading POP/DMD mode from year-round ERA5 data from 1979–2020. Contour lines show the (a) EOF1 and (b) EOF2 patterns. Blue and dashed lines indicate negative values, i.e., easterlies (zero lines are omitted). (c, d) The same as panels (a) and (b) but for the idealized GCM with a propagating regime. In panels (a)–(d),  $\lambda_R$  and  $\lambda_I$  are the real and imaginary parts, respectively, of the eigenvalue associated with the POP/DMD mode. The periodicity of each mode is  $2\pi/\lambda_I \approx 150$  days. The periodicities of the leading POP/DMD modes in panels (a) and (b) and (c) and (d) closely match the periodicities that were theoretically predicted using Eq. (7); see Table 1. (e) The POP/DMD mode (shading) that most closely resembles EOF1 (contour lines). This POP/DMD mode is real and has a real eigenvalue. (f) The same as panel (e) but for EOF2. This mode is also real. See Materials and Methods for more details about the reanalysis data and idealized GCM setups, and Appendix A for details about the POP/DMD analysis. Figure S6 shows the same analysis but for three other reanalysis products.

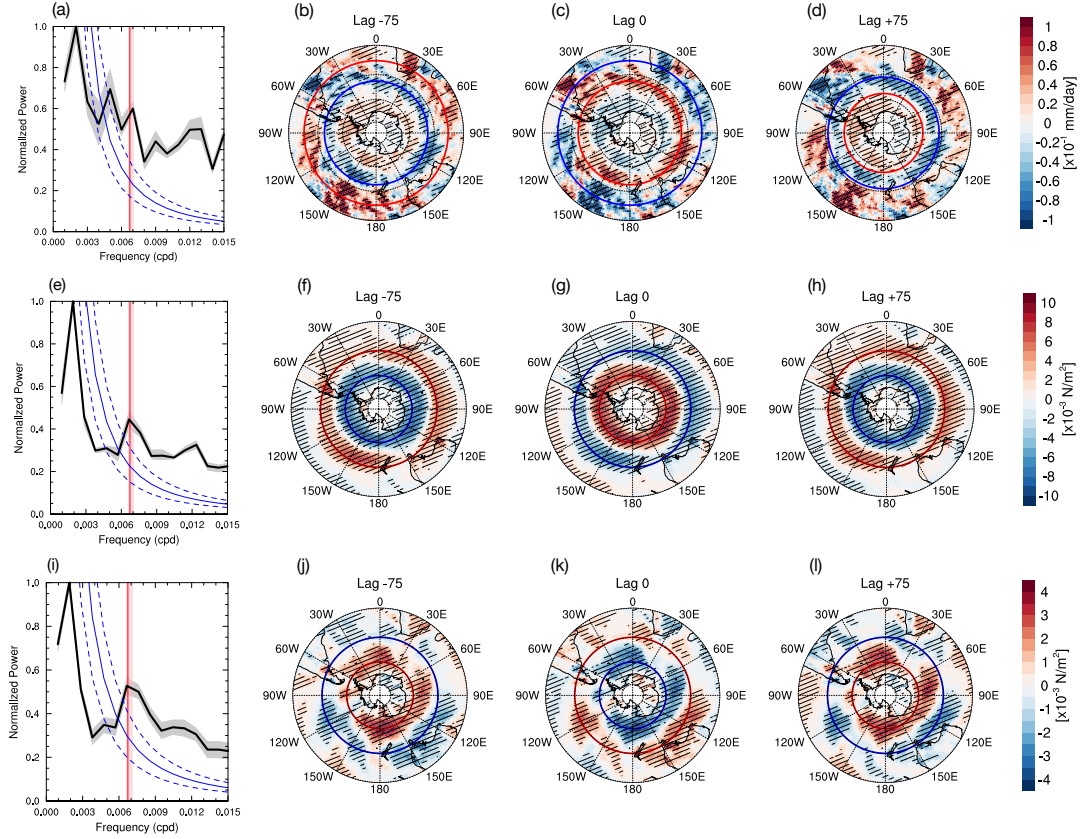


**Figure 3.** Periodicity in Southern Hemisphere precipitation and surface wind stress. Spectra of the zonal-mean (a) vertically averaged (total) precipitation, (e) zonal wind stress, and (i) meridional wind stress. Precipitation data are from year-round ERA5 data from 1979–2020 and wind stress data are from year-round NCEP1 data from 1979–2020. The power spectra are calculated for hemispheric averages ( $20^{\circ}\text{S}$ – $80^{\circ}\text{S}$ ) of the anomalous fields. The grey shading represents the standard error of the mean; it was computed as the 5% and 95% confidence intervals of the bootstrapped distribution across trials. The red-noise spectra are indicated by the solid blue lines and the dashed blue lines are the 5% and 95% a priori confidence limits. The red vertical line and its shading show the mean and 25th–75th percentiles of the theoretically predicted periodicity from Eq. (7), which is  $\sim 150$  days; see Table 1. The remaining panels show the lagged composited differences for (b–d) anomalous total precipitation, (f–h) zonal wind stress, and (j–l) meridional wind stress. The composites are computed by first averaging the anomalies at lags of 0,  $-75$ , or  $+75$  days with respect to dates at which the 140–160-day band-pass-filtered  $z_1$  reaches local maxima or minima, and then calculating the difference (maxima minus minima) for each lag. Composites are shown southward of  $20^{\circ}$  and hatching indicates statistical significance at the 95% level based on a  $t$ -test. See Materials and Methods and Supporting Information for more details about the data and spectral analysis of the time-series, and Appendix B for details about the composite analysis.



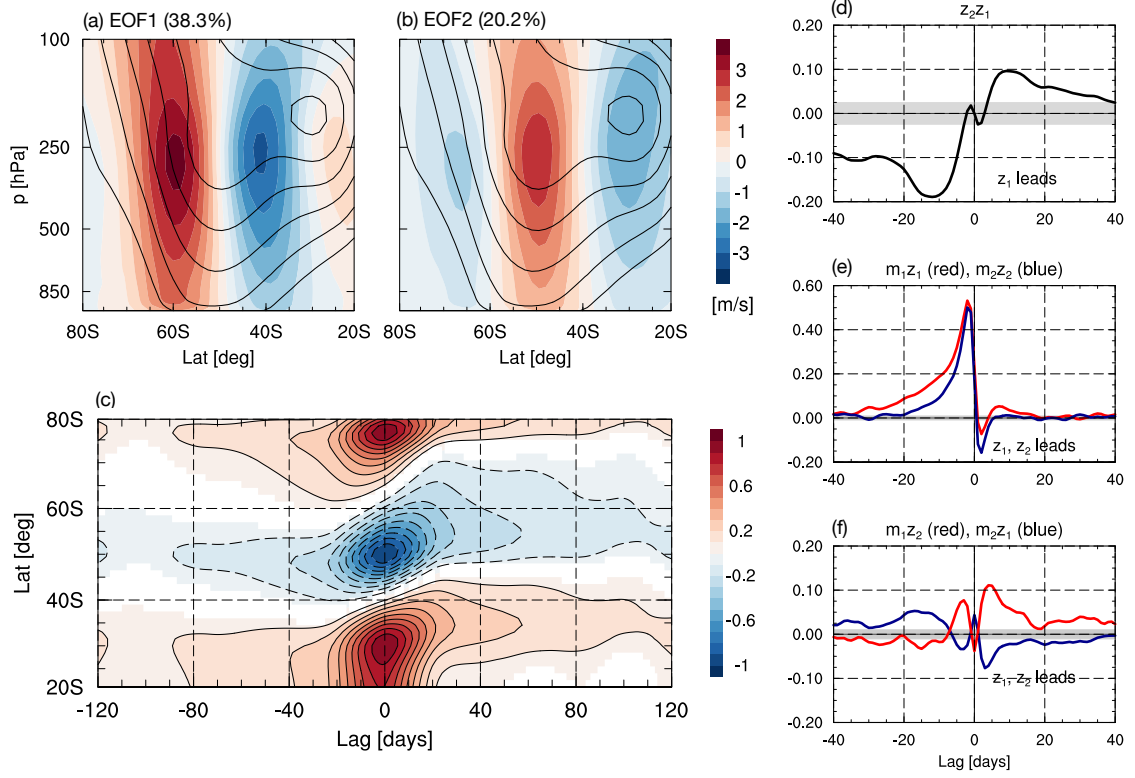


**Figure 4.** The Southern Annular Mode (SAM) in ERA5 reanalysis data. (a, b) Shading shows the patterns of EOF1 and EOF2, which are the two leading EOFs of zonal-mean zonal wind anomalies in the Southern Hemisphere from year-round ERA5 data from 1979–2020. The two leading EOFs contribute 38.3% and 20.2% to the total variance, respectively. The contour lines represent the climatological zonal-mean zonal wind with an interval of 5 m/s. (c) One-point lag-correlation map of the zonal-mean zonal wind anomalies integrated across the depth of the troposphere (1000–100 hPa), reconstructed from projections onto the two leading EOFs of the zonal-mean zonal wind anomalies. The base latitude is at 30°S, which is the position of the maximum negative wind anomalies of EOF2 at low latitudes; see panel (b). Contour lines have intervals of 0.1, dashed lines indicate negative values, and zero lines are omitted. Shading shows values that are significant at the 95% level based on a  $t$ -test. (d) Cross-correlation between the PCs,  $z_1(t)$  and  $z_2(t)$ . (e) Cross-correlation between  $m_1$  and  $z_1$  (red) and  $m_2$  and  $z_2$  (blue). (f) Cross-correlation between  $m_1$  and  $z_2$  (red) and  $m_2$  and  $z_1$  (blue).  $m_1(t)$  and  $m_2(t)$  are the eddy momentum forcing time series, computed as the eddy momentum flux divergence regressed onto  $z_1$  and  $z_2$ , respectively. Note that in panels (d)–(f), the  $y$  axes have different ranges for better illustration. In these panels, the grey shading represents the 5% significance level according to the Bartlett test. Note that the ratio of the EOF1 to EOF2 explained variances is 1.9 and the climatological jet structure are consistent with the rule of thumb for the existence of the propagating regime of annular modes: the ratio should be  $< 2$  and there should be a double-jet structure (Son & Lee, 2006; Son et al., 2008; S. Lee et al., 2007). See Materials and Methods and the Supporting Information for more information about the reanalysis data, the calculation of  $z$  and  $m$ , one-point lag-correlation maps, and the Bartlett test.

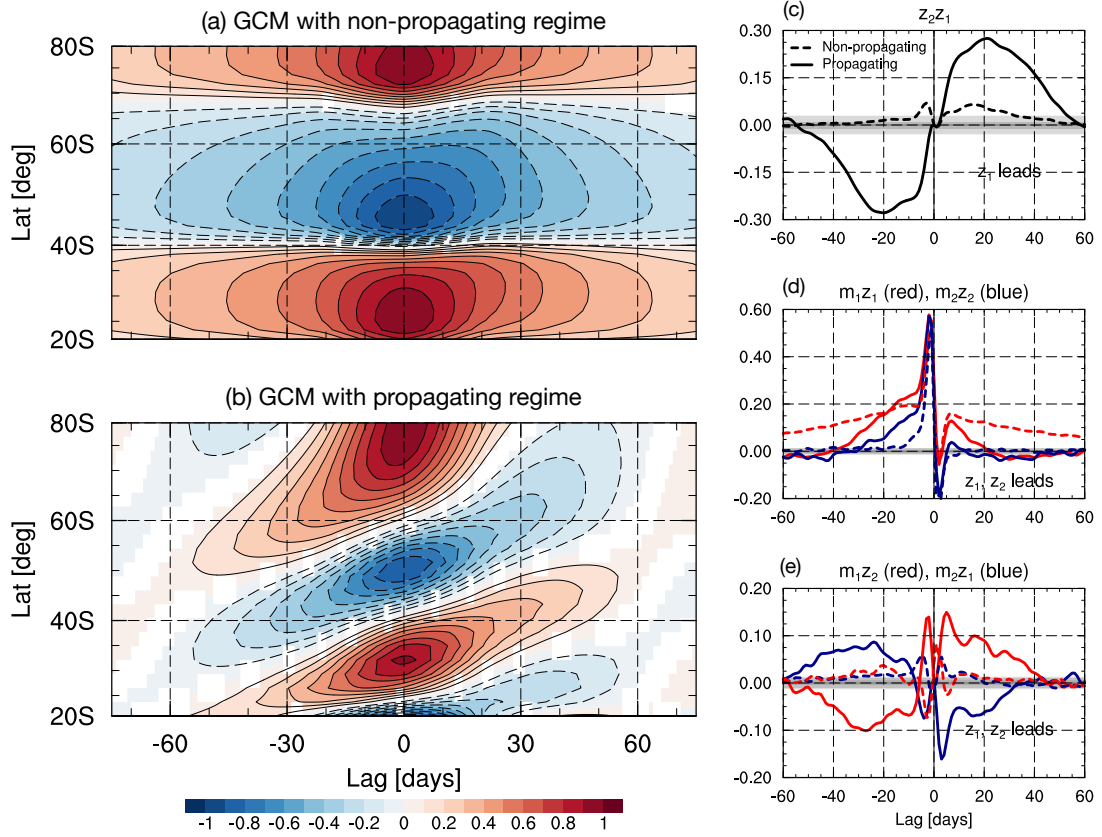


**Figure 5.** Propagating and non-propagating annular modes in two idealized GCM setups. The two setups of the idealized GCM (a dry dynamical core), with one producing the propagating regime and the other producing the non-propagating regime of the annular modes, are described in Materials and Methods (the patterns of EOFs and climatologies are shown in Fig. S3). (a, b) One-point lag-correlation map, similar to Fig. 4c, for the setup with the non-propagating regime (top) and the setup with the propagating regime (bottom). The base latitude for the one-point lag-correlation map is  $32^{\circ}\text{S}$  ( $25^{\circ}\text{S}$ ) for the propagating (non-propagating) regime; it was chosen as the location of the maximum negative wind anomalies of EOF2 at low latitudes (see Fig. S3). Using the same base latitude of  $30^{\circ}\text{S}$  for both setups leads to qualitatively similar maps (Lubis & Hassanzadeh, 2021). See the caption of Fig. 4 for information about the contour lines and shading. (c) Cross-correlation of  $z_1$  and  $z_2$ . (d) Cross-correlation of  $m_1$  and  $z_1$  (red) and  $m_2$  and  $z_2$  (blue). (e) Cross-correlation of  $m_1$  and  $z_2$  (red) and  $m_2$  and  $z_1$  (blue). In panels (c)–(e), solid and dashed lines indicate the propagating and non-propagating regimes, respectively. As in Fig. 4, grey shading represents the 5% significance level according to the Bartlett test. See Materials and Methods and the Supporting Information for more information about the idealized GCM setups, the calculation of  $z$  and  $m$ , one-point lag-correlation maps, and the Bartlett test.

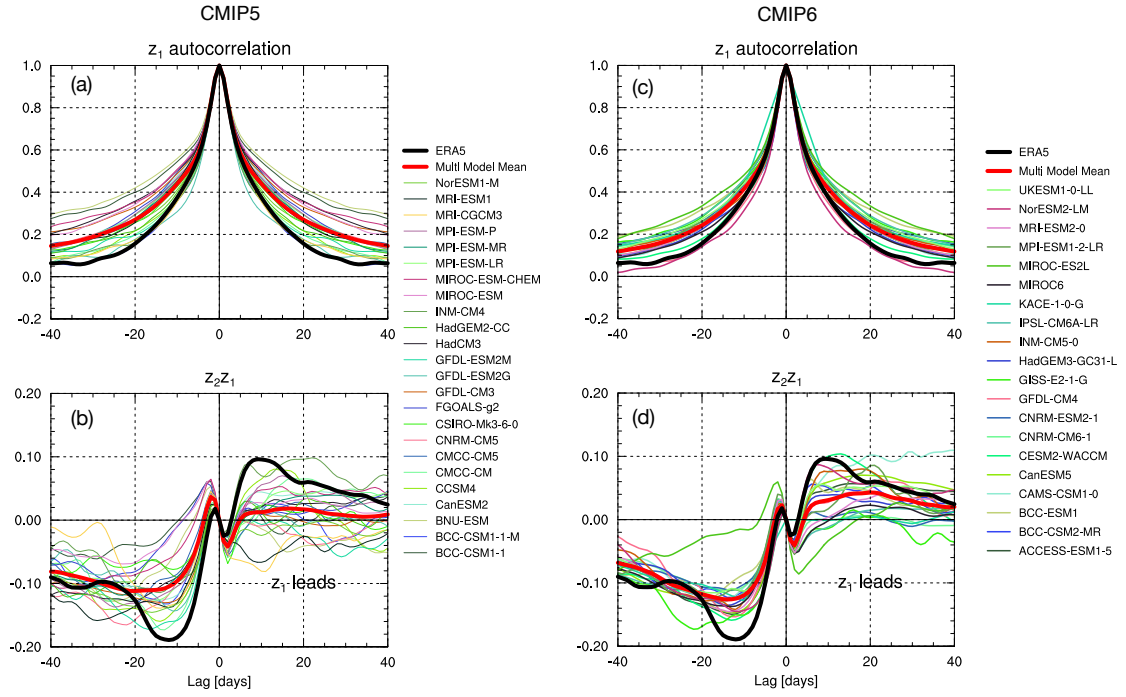


**Figure 6.** The autocorrelation function of the Southern Annular Mode (SAM) zonal index and the cross-correlation between the PCs of EOF1 and EOF2 in the CMIP5 and CMIP6 models. (a, c) Autocorrelation function of  $z_1$ , and (b, d) cross-correlation of  $z_1$  and  $z_2$ . The thin lines indicate individual models, the thick red lines indicate the multi-model mean, and the thick black lines indicate ERA5 reanalysis. See Materials and Methods and the Supporting Information for more details about the CMIP models and the calculations of  $z_1$  and  $z_2$  time-series.

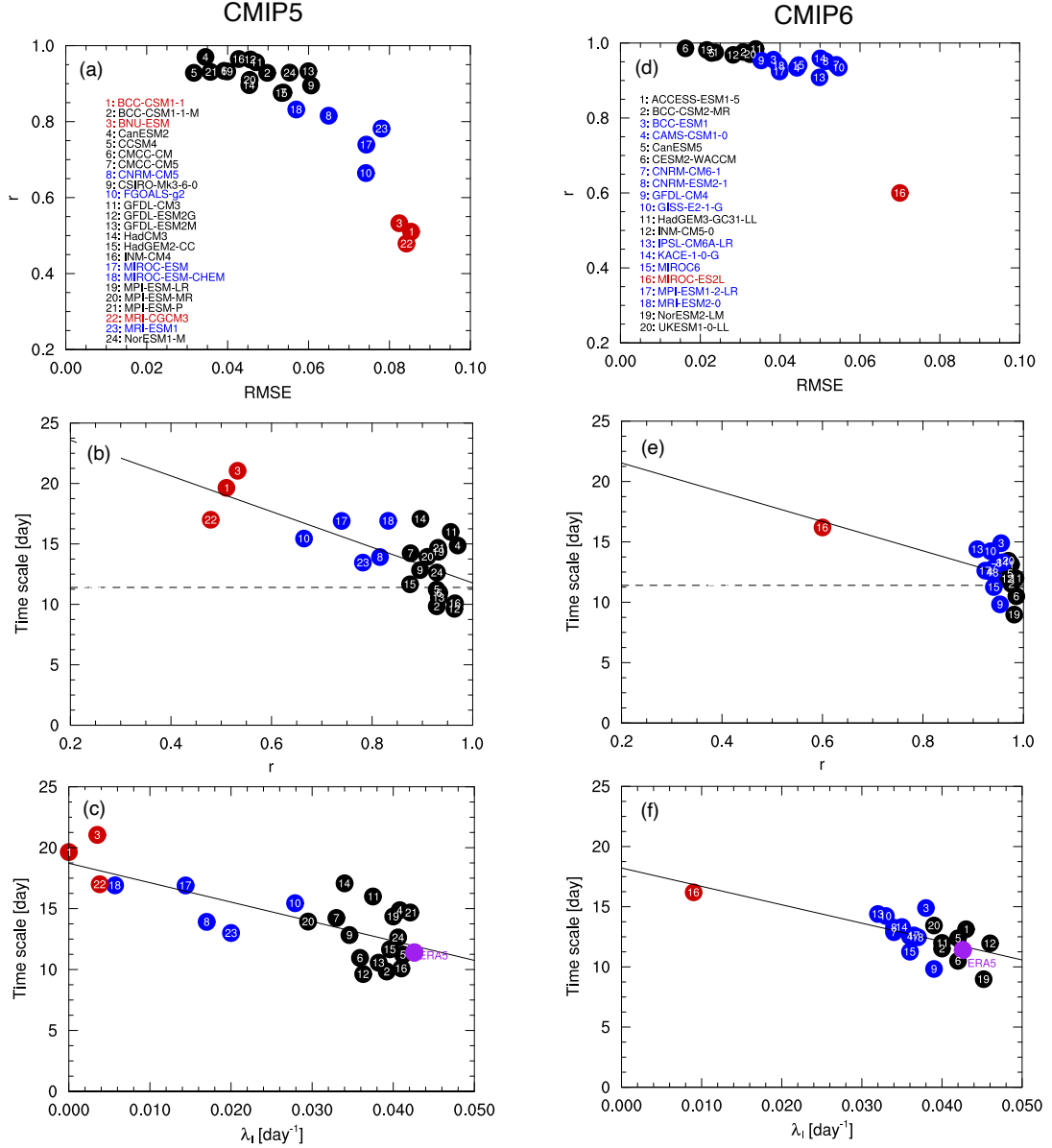


**Figure 7.** The impact of the quality of the simulated propagating regime on the SAM persistence in CMIP5 and CMIP6 models. (a, d)  $k$ -means cluster analysis of  $r$  and RMSE values for each model. The higher (smaller) the  $r$  (RMSE) value, the better the model is at simulating the propagating regime. (b, e) Relationship between  $r$  and the  $e$ -folding decorrelation timescale of  $z_1$  (commonly used as the measure of persistence (Gerber, Voronin, & Polvani, 2008; Gerber, Polvani, & Ancukiewicz, 2008)). The horizontal dashed line indicates the timescale in ERA5. (c, f) Relationship between  $\lambda_I$  from the POP/DMD analysis and the decorrelation timescale.  $\lambda_I$  is the imaginary part of the eigenvalue of the POP/DMD mode corresponding to the propagating annular mode, indicating the period of the propagating SAM (see Materials and Methods and Appendix A).